UNIVERSITY OF OKLAHOMA GRADUATE COLLEGE

FOAM-TEMPLATED POROUS HYDROGELS: TUNING STRUCTURE AND WATER UPTAKE KINETICS

A THESIS

SUBMITTED TO THE GRADUATE FACULTY

in partial fulfillment of the requirements for the

Degree of

MASTER OF SCIENCE

By SARAH ONYEMBE

Norman, Oklahoma

2025

FOAM-TEMPLATED POROUS HYDROGELS: TUNING STRUCTURE AND WATER UPTAKE KINETICS

A THESIS APPROVED FOR THE

SCHOOL OF SUSTAINABLE CHEMICAL, BIOLOGICAL, AND MATERIALS ENGINEERING

BY THE COMMITTEE CONSISTING OF

Dr. Reza Foudazi, Chair

Dr. Michele Galizia

Dr. Mrinal Saha

DEDICATION

This thesis is dedicated to my beloved mother, siblings, and wonderful cousin for their unwavering love and support throughout my journey as an aspiring researcher. I would not be where I am today without you.

ACKNOWLEDGEMENTS

I would especially like to thank my thesis supervisor, Dr. Foudazi, for his guidance, insightful advice, and patience. From the time I started as an undergraduate researcher in my sophomore year in October 2021, he has been a great mentor and an inspiring figure whom I look up to in my academic journey and my future professional life. This research will be fundamental to the publication we are working on.

I would also like to extend my gratitude to our research group, the Soft Matter Research and Technology (SMaRT) Group, for their continuous feedback during our group meetings. Their valuable suggestions and constructive criticism have played a crucial role in improving my research.

A special thank you to my committee members, Dr. Michele Galizia and Dr. Mrinal Saha, for their support and words of encouragement throughout the process of writing my dissertation. I also want to acknowledge Sydney Hulen, the undergraduate student I had the opportunity to mentor this semester, for her contributions, which will be instrumental in shaping the future direction of this research.

My research would not have been possible without the support of the Samuel Roberts Noble Microscopy Laboratory, where Dr. Preston Larson assisted me in capturing high-quality SEM images of my hydrogels. Additionally, I am deeply grateful to the Undergraduate Research and Creative Activity (UReCA) program at OU, which provided financial support over the summer, allowing me to dedicate myself fully to this project. Through UReCA, I was also given the opportunity to participate in panel events and share my research beyond Oklahoma.

I am incredibly thankful for my friends, who have made my master's experience more enjoyable and memorable. Above all, I would like to express my deepest gratitude to my mother Regine, siblings, and cousin for their unconditional love, support, and encouragement. Their belief in me has been a driving force, and I truly would not be where I am today without them.

Finally, there are so many people I am grateful for, and countless small acts of kindness that have helped me along this journey. To every one of you, thank you.

ABSTRACT

Foam templated porous polymers, which are also called polyfoams, have applications in food packaging, energy storage, sustainable agriculture, and plant growth in outer space. These materials are highly versatile due to their lightweight properties and tunable mechanical characteristics. Despite their advantages, polyfoams face challenges such as low water uptake and foam stability issues, where controlling foam stability prior to polymer network formation remains a challenge that limits further scientific exploration in this field. Achieving small pore sizes (less than 100 μm) is crucial for enhancing properties like thermoresponsiveness and water uptake kinetics. Another key challenge is controlling porosity to fine-tune the hydrogels for specific applications. This study explores the interactions between the block copolymer Pluronic F68 Diacrylate (PF68DA) and sodium dodecyl sulfate (SDS), which are used as the macromer and co-surfactant in the precursor, respectively. The goal is to understand how SDS influences foam stability and interfacial dynamics and how these factors affect the final porosity and properties of polyfoam hydrogels obtained from the crosslinking of PF68DA. Our findings reveal that SDS reduces both pore (also known as void) and pore throat (also known as window) sizes in the resultant porous hydrogels. At elevated SDS concentrations, destabilization occurs due to increased depletion attraction forces, leading to the formation of more windows with smaller void sizes in the final hydrogel structure. While these hydrogels exhibit lower mechanical strength compared to non-porous hydrogels, their mechanical properties remain comparable to polyfoams reported in literature. Additionally, this research further confirms that introducing foaming significantly enhances thermoresponsiveness and water uptake kinetics compared to non-foamed (i.e., dense) hydrogels.

TABLE OF CONTENTS

LIST OF TABLES

LIST OF FIGURES

1 Introduction

1.1 Introduction To Porous Hydrogels and Polyfoams

As three-dimensional cross-linked hydrophilic polymer networks, hydrogels swell in water and possess properties such as biocompatibility and biodegradability. Porous hydrogels contain physical pores besides the space available between adjacent cross-links in the polymer network. This structure makes them excellent for adsorption, absorption, and controlled delivery in various applications, such as biomedical and tissue engineering (1–3), cosmetics (4), drug delivery (5), clean water production (6), and agriculture (7), while maintaining structural integrity. Among the different types of porous hydrogels, foam-templated are unique, characterized by a distinctive dual-porosity structure, consisting of closely arranged percolated macropores (> 50 nm) usually on the order of 100 μm and sometimes micropores (< 1.4 nm)(8,9). They are usually referred to as polyfoams, offering low density, a large surface-to-volume ratio, and tunable mechanical properties (10).

In contrast to non-porous hydrogels, where water diffuses into the network, foam-templated hydrogels absorb water primarily through capillary action facilitated by open pores, making their water uptake faster. By comparison, closed-cell porous hydrogels swell more slowly due to limited pore interconnectivity, where water must diffuse through the polymer matrix or isolated voids (1,11) as seen in Figure 1-1. Foams have been used as templates for porous hydrogels to control their morphology by modifying the liquid foam before polymerization. The pores originally filled with gas in the template become filled with water in the final swollen polyfoam. The pore size and porosity of foam-templated hydrogels can be tuned by different process parameters such as the mixing geometry, the mixing speed and time, the amount of gas injected, and the volume of the

sample, to name a few, enabling control over water uptake kinetics, thermal responsiveness, and mechanical behavior (1). Generally, the preparation of porous hydrogels by the foam-templating method can be classified into different main categories as seen in Table *2-1*. They will be discussed later.

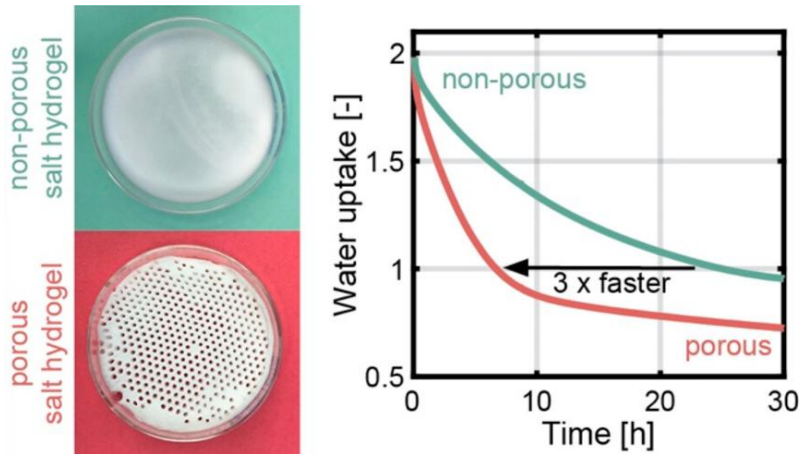

Figure 1-1. Comparison of water uptake between porous hydrogels and non-porous hydrogels (12)

1.2 Significance of Studying Polyfoams

Porous hydrogels, specifically polyfoams, have applications in solar water purification (23), energy storage applications (9,24) as seen in Figure *1-2* (a), regenerative medicine, and scaffolds (25,26), 3D materials in cell growth (27,28), and additives to keep moisture contributing to plant growth (29,30), to name a few. Compared to conventional hydrogels, polyfoams can be engineered to have good mechanical stability (19) and elasticity as seen in Figure *1-2* (b), properties that are crucial in tissue engineering, flexible electronics, and soft robotics applications. Additionally, due to their highly interconnected structure, they can be used in catalysis (22) and filtration applications (23). A key application explored in this research is the potential use of these porous hydrogels in space farming and sustainable agriculture, where they

can serve as materials capable of absorbing and releasing water and nutrients under microgravity conditions as seen in Figure *1-3* a&b. With the growing interest in space exploration, such adaptable materials could be vital in sustaining plant growth beyond Earth (7).

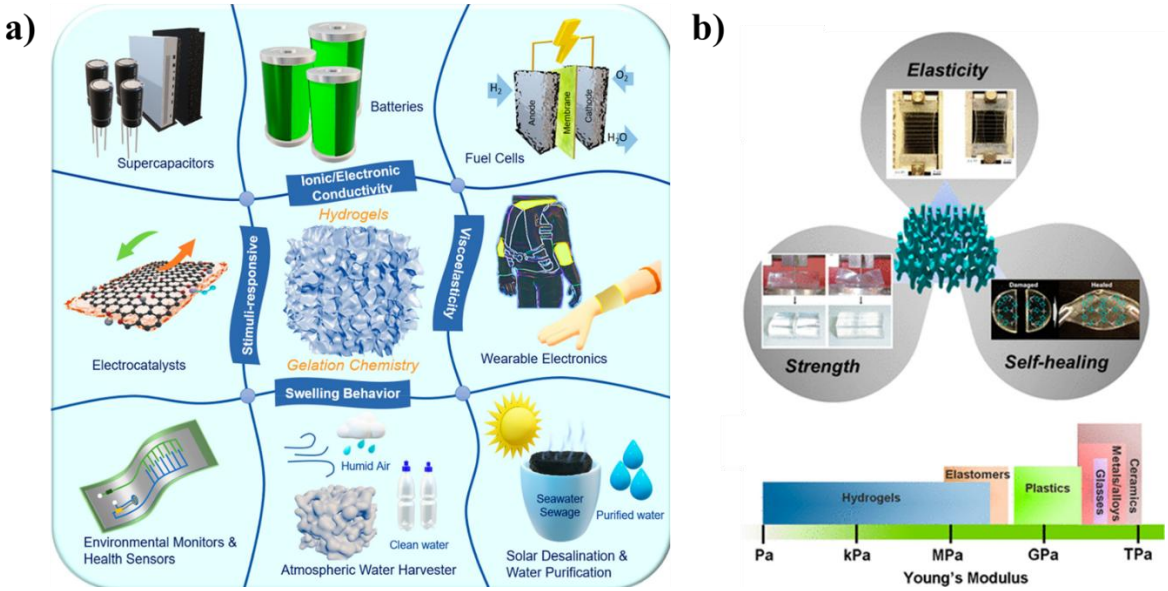

Figure 1-2. Summary of energy applications related to hydrogels on the left, along with some of their mechanical properties on the right: (a) shows hydrogel properties, while (b) compares them to other materials, highlighting that hydrogels are among the softest materials (24).

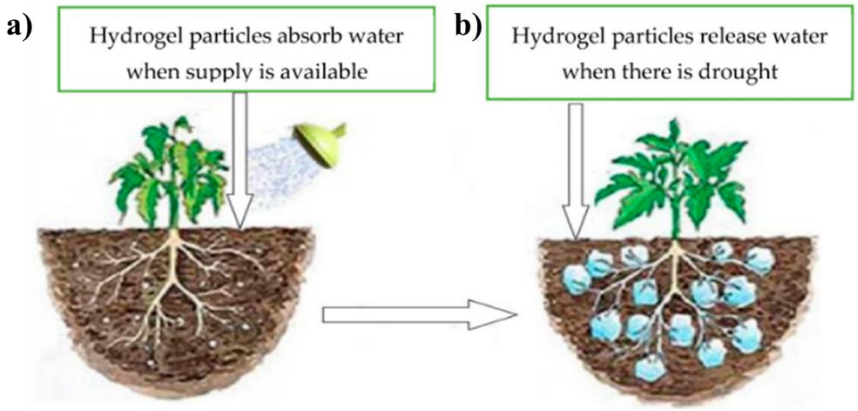

Figure 1-3. Hydrogel absorbs water (a) upon addition of water to the plant and (b) hydrogel releasing water in drought condition (7).

1.3 Research Objectives and Hypotheses

Our research hypothesis is that by controlling the interaction between polymer (macromer) and surfactant, we can tune and control the properties and structure of the foam-templated porous hydrogels and improve their performance. With that in mind, our study aims to comprehensively investigate the role of SDS in modifying the structural and functional properties of polyfoam hydrogels synthesized from PF68DA. PF68DA is both a surfactant and a macromer, and SDS plays the role of a cosurfactant in this case. The first objective focuses on micelle formation and the interaction of SDS with PF68DA, emphasizing how varying SDS concentrations impact surface tension. Understanding these interactions is critical for optimizing cosurfactant-polymer systems to enhance stability and performance in templating processes.

The second objective delves into foam stability, a crucial factor in polyfoam hydrogel formation. By employing optical microscopy and interfacial dilatational rheology, this study aims to characterize the impact of surfactants on foam lifespan and the presence of any micelles at the air-liquid interface. These findings will provide insight into the mechanisms governing foam stability and help refine the formulation of polyfoams with optimized properties.
The third objective focuses on the physical characterization of the resulting polyfoam hydrogels. Scanning electron microscopy (SEM) will be utilized to assess the porosity, pore size distribution, and pore interconnectivity of the foam structures. Additionally, compression testing will be conducted to evaluate the mechanical strength of the polyfoams, which are essential for determining their suitability for various practical applications, including biomedical and agricultural uses.

Finally, the fourth objective explores the functional performance of polyfoam hydrogels by analyzing their swelling kinetics, water uptake behavior, and thermoresponsive properties.

Understanding these aspects will allow us to make the hydrogels more adaptable for targeted applications such as controlled drug release, smart agricultural materials, and temperature-sensitive scaffolds. Collectively, these objectives contribute to the broader goal of developing high-performance porous hydrogels with tunable properties for various applications.

To address these objectives, we develop microcellular foam-templated porous hydrogels using a nitrogen gas foaming process as described in Zowada et al. (25), offering a cost-effective and material-efficient method to control structure, swelling behavior, and thermoresponsiveness. This approach achieves small void sizes (≤ 25 μm) while minimizing material use by combining PF68DA and SDS as the primary components. PF68DA served as a monomer, crosslinker (after diacrylation), and surfactant, reducing the need for additional chemical crosslinkers. SDS, as a co-surfactant, can facilitate the stabilization of bubbles and the decrease of dissolution of nitrogen in the water. PF68DA and SDS have been reported to have a strong interaction represented by a pearl-necklace structure (31). The polymerization is initiated using UV light, enabling precise network formation. Before and after polymerization, the effects of surfactant concentration on the structure, including morphology and bubble/pore size distribution, are systematically investigated. The relationship between SDS and PF68DA is further understood through micelle size changes and foam formation analysis at different surfactant concentrations using optical microscopy, while polymerized samples are characterized by SEM. The relationship between interfacial rheology and stability of the foam is also elucidated.

1.4 Layout of Research

Polyfoams are versatile materials that can be applied in a wide range of applications. The remainder of this thesis includes a few more chapters. Chapter 2 provides a comprehensive literature review on polyfoam hydrogels, covering the various production methods, formulations

reported in the literature, foaming agents used in their synthesis, and the key properties of previously studied polyfoam hydrogels. This review establishes the foundation for understanding the role of surfactants in hydrogel formation and stability. Chapter 3 will present an outline of the materials, methods, and equipment used to achieve the research goals of this project. Chapter 4 presents the core findings, focusing on the interaction between PF68DA and SDS. It examines how this interaction influences hydrogel properties, including surface activity, micellization, and foam stability. The chapter also explores the effects of a co-surfactant on hydrogel morphology and porosity through imaging and mechanical characterization. In Figure 1-4, you can see the length of the scale for this project. Finally, Chapter 5 will summarize the key conclusions of this research and discuss future directions. This section will highlight potential improvements, unanswered questions, and the broader implications of the findings for hydrogel applications in the agriculture field for outer space applications.

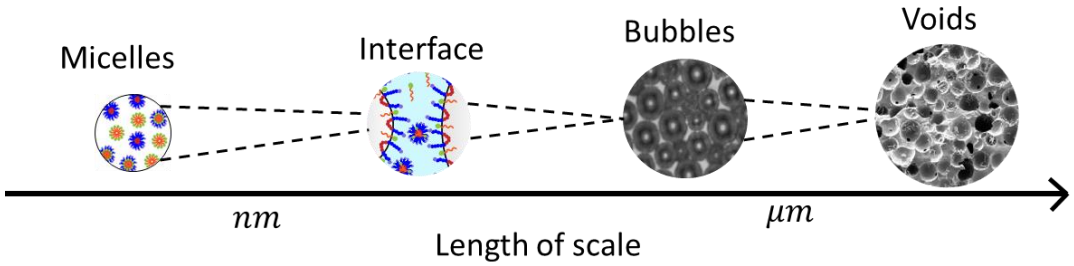

Figure 1-4. Length of scale for this study

2 Literature Review

2.1 Methods to produce Porous Hydrogels

Typically, the liquid foam template consists of a mixture of monomer, solvent (water), emulsifier/stabilizers, and initiator that will be solidified by crosslinking to produce the solid

porous hydrogel (6,11). Surfactants are used to reduce the surface tension and stabilize the foam templates prior to crosslinking (12,13). Foam is typically considered an air-in-liquid dispersion and based on the liquid volume fraction ϕ, the foam can be classified as "dry foam" or "wet foam". When $\phi < 0.05$, then the system is a "dry foam" and when $\phi < 0.36$, we have a "wet foam". The value 0.36 is the critical volume fraction (ϕ_c) of unoccupied space in packing of spheres for polydispersed foams (25). When $\phi > \phi_c$, we have a "bubbly liquid" (9). Foam templating can be done by both dry and wet foams, although the latter is more accessible. Several methods can be employed to produce the liquid foam used to generate foam-templated porous hydrogels. Generally, the preparation of porous hydrogels by the foam-templating method can be classified into these main categories as seen in Table 2-1.

Table 2-1. Summary of methods used for producing foams (14–16)

Method	**Foaming agents**	**Advantages**	**Challenges**
Physical Foaming	Volatile solvent or gas such as supercritical CO_2, N_2 and 1-butane in extrusion	Low cost for agents. Pollution-free. No further washing is required. Simple, cheap, eco-friendly, minimal processing.	Special injection molding machine. Sensitive to mixing speed and foam aging.
Chemical Foaming	Chemical blowing agents (water, H_2, O_2)	Thermally decomposed within	High mold manufacturing precision.

	that can decompose into gas when exposed to temperatures that promote foaming	a specific temperature range. Releases gases within polymer resins. Works with standard, cost-effective injection molding machines.	Expensive mold. Requires additional clamping pressure device for high-pressure foaming.
Mechanical foaming (25) **(This study)**	Air is dispersed by mechanical stirring (mechanical frothing)	No additional foaming agent. Easy to operate and automate. Non-toxic and safe. Lower cost and efficiency. No additional washing.	Lower requirements on equipment. Special injection molding machine. Less effective in high-viscosity solutions.
Freeze-Drying	Water or solvent frozen in the polymer solution and sublimated under a vacuum	Tailored size. Non-toxic solvents.	Costly. Time-consuming. Limited scale.

Emulsion Templating	Immiscible liquids stabilized by surfactants or other emulsifiers	Better control over the pore size. High porosity achievable.	More complex post-polymerization process. Requires surfactants for stabilization.
Microfluidics	Nitrogen or other gases through microfluidic channels	Reproducible void structures. Precise control over pore size.	Limited scalability due to lower production rates. Requires costly microfluidics devices on a large scale.

As seen in Table *2-1*, mechanical foaming is one of the most resource-efficient methods. It is often preferred over techniques like emulsions because it replaces the internal liquid phase with a gas, eliminating the need for post-polymerization washing or extraction steps. This method requires no special equipment and uses minimal toxic chemicals or solvents (9). Additionally, it is considered environmentally friendly as it relies on air as the dispersed phase, minimizing contamination.

In general, the methods of production for porous hydrogels can be classified into two main methods: kinetic and templating as shown in Figure 2-1. In kinetic methods, the microstructure is allowed to evolve dynamically over time while in templating method, the final porous structure is an exact replicate of the original template used (9). Kinetic methods include

bubble generation from a reaction, 3D printing, freeze drying, phase separation, electrospinning, and sintering. Templating methods, also referred to as colloidal templating methods, include emulsion templating, foam templating, solvent casting with particle leaching (1), and self-assembly templating (23). The main challenge in kinetic methods is achieving independent control over porosity and pore size. In templating methods, retaining the templated structure is not always feasible (9). Combining some of these techniques can create structures at different length scales, leading to improved properties. (11).

Foams are often preferred over other techniques, such as emulsions, because the internal liquid phase present in emulsions is replaced by a gaseous phase in foams. Additionally, the template remains in the final porous structure, eliminating the need for post-polymerization washing or extraction. Foam templating also requires no special equipment and minimizes the use of toxic chemicals and solvents, unlike those produced via emulsion-templating techniques (3,9). Additionally, it is considered environmentally friendly, as it uses gases such as nitrogen as the dispersed phase and water as the continuous phase, reducing the risk of contamination.

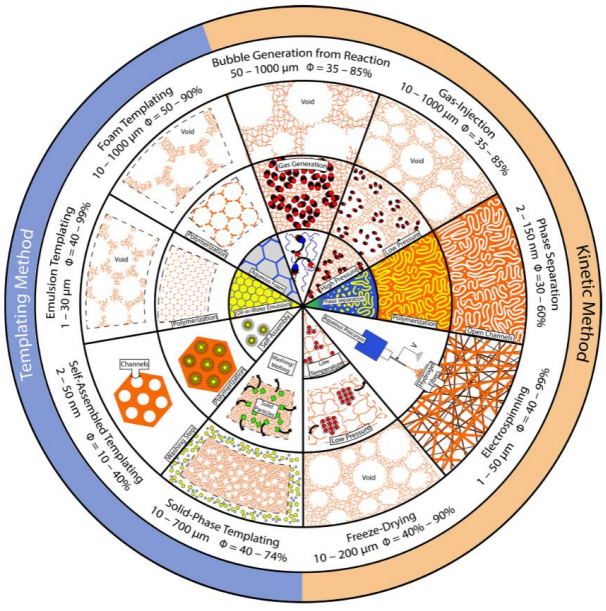

Figure 2-1. Summary of methods used to produce porous hydrogels (9)

2.2 Previous Studies on Polyfoam Systems

Several papers have addressed issues related to instability of foams prior to crosslinking by exploring different types of stabilizers. Nanoparticles can serve as stabilizers, as demonstrated by Tan et al., who reported the production of a polymer foam using silica nanoparticles hydrophilized by CTAB and cured through thermal-initiation polymerization. They successfully retained the template after polymerization, as the bubble sizes were similar to the pore sizes of the polymerized foam (32). Graphene oxide can also be used as a stabilizer and has been proven to be a very efficient Pickering stabilizer, especially in emulsion templating (33). Reports on surfactant-stabilized foams have also been published. Shi et al. investigated the effect of surfactants on the porosity and swelling behavior of superabsorbent hydrogels and found that SDS enhances the swelling rate and provides good thermoresponsive properties to the hydrogel (12). In addition to stability issues, achieving void sizes smaller than 100 μm with mechanical frothing remains challenging due to the difficulty in controlling void size and polydispersity, which makes reproducibility unreliable. Similarly, in the foam-templating method, the strong aging effects of bubbles in the system, often occurring before polymerization is complete, further complicate the process (10).

A recent study on foam-based hydrogels explored dual surfactant systems to enhance pore structure, swelling behavior, and mechanical properties. The study by Pinthong et al. (21) investigated the effects of combining a nonionic surfactant, Pluronic F127 (PF127), with an anionic surfactant, SDS, as well as another combination using Tween 20 instead of SDS (21). The primary focus of this study was on wound dressings, which require moderate to heavy exudate absorption, superior moisture retention, and the ability to incorporate bioactive agents. The monomer used, 2-acrylamido-2-methylpropanesulfonic acid (AMPS), was selected due to its

high-water absorption capacity and ionic conductivity. To fabricate the porous hydrogels, the researchers employed a gas-blowing technique, a chemical foaming technique, which allows gas bubbles to be generated inside the material during the gelation process. These gas bubbles act as porogens for controlled pore formation. In this method, gas is produced within the hydrogel precursor during gelation, with N,N,N′,N′-tetramethylethylenediamine (TEMED) and ammonium persulfate (APS) acting as redox initiators. Surfactants played a crucial role in stabilizing the foam by reducing surface tension, forming a lamellar film that stabilized the foam, and preventing coalescence to ensure a uniform and interconnected porous structure.

Pinthong et al. found that the 50%PF127:50%Tween 20 and 80%PF127:20%SDS compositions produced the most uniform and interconnected pores, with average pore sizes of 25.61 ± 8.99 μm and 29.72 ± 8.53 μm, respectively. Hydrogels synthesized with only a single surfactant exhibited larger, less stable pores, leading to weaker mechanical properties. The 50%PF127:50%Tween 20 hydrogel demonstrated the highest swelling capacity, absorbing up to 5730% of its weight in water. The study also revealed that higher porosity with smaller pores improved swelling behavior due to enhanced capillary action. Moreover, dual surfactant systems exhibited better foam stability during gelation, whereas single surfactant formulations led to irregular, weaker foams. These formulations also enhanced mechanical properties, with a high storage modulus of 4758 Pa in the dry state and 1541 Pa in the wet state, indicating improved structural integrity.

A related study by Zowada et al. focused on single-surfactant-based hydrogels using PF68 as the main surfactant (25).Their foaming method involved two interconnected syringes containing an aqueous phase and nitrogen (N_2), where gas was injected into the solution and subjected to back-and-forth movement to induce bubble breakup. Similar to Pinthong et al.,

AMPS was used as the monomer, and APS/TEMED served as the redox initiators. However, their results showed that foam-based hydrogels exhibited lower swelling uptake compared to high-internal-phase emulsion (HIPE) hydrogels. These hydrogels also demonstrated very low mechanical strength, which is expected from highly porous materials. Additionally, the foam stability was limited, with coalescence and bubble collapse occurring within 1-2 hours. They were able to achieve an average void diameter of 38.5 μm at 50% porosity.

Building on these findings, this research focuses on modifying PF68 by diacrylation to create a polymerizable macromer while using SDS as a co-surfactant to control porosity and tune hydrogel properties. The goal is to develop a cost-effective method to fabricate polyfoam hydrogels with optimized structure and swelling behavior, making them highly adaptable for agriculture applications in the outer space as well as other biomedical and industrial applications**.**

2.3 RESEARCH GAPS

As seen in Table 2-1, from all the methods above, mechanical foaming is usually the lowest cost and does not require a lot of resources to operate. The foam-templating method has yet to gain widespread popularity due to several challenges. A significant issue is maintaining the foam structure after polymerization while achieving smaller pore sizes, especially less than 100 μm, because of the strong aging effect in the foam which leads to larger bubbles and voids (10). Additionally, developing high-performing porous hydrogels with fewer materials remains a critical challenge. To preserve pore size and porosity, it is crucial to cross-link the liquid foam quickly before coalescence occurs. The competition between foam instability mechanisms, such as gas diffusion, Ostwald ripening, coalescence, and drainage, and crosslinking kinetics often compromises the foam structure during the templating process. Furthermore, most hydrogels exhibit low mechanical strength, and the introduction of porosity often worsens this limitation.

Given the need to design more cost-effective products with fewer materials and develop versatile porous hydrogels, it is essential to explore innovative techniques to address these challenges.

3 Materials and Methods

3.1 Materials

PF68 (Mw = 8400 g/mol), acryloyl chloride, toluene, dichloromethane, hexane, and triethylamine were purchased from Sigma-Aldrich. PF68 was diacrylated, using all the materials listed in the previous sentence, following the method described in Sabbat et al.'s paper (35) and is referred to as PF68DA in this paper. The UV photoinitiator Omnirad 2959 (formerly known as Irgacure 2959) was obtained from iGM Resins. SDS with 99% purity (CAS 151-21-3) was acquired in micropellet form, molecular biology grade, from Fisher BioReagents. Ultrapure deionized water was prepared using a Millipore Synergy® Water Purification System to ensure the high purity and quality required for experimental procedures.

3.2 Diacrylation

The diacrylation of PF68 involves a two-day process. The reaction scheme can be found below in Figure 3-2. On day one, 50 grams of PF68 is dissolved in a mixture of 30 mL toluene and 100 mL dichloromethane (DCM) in a sealed reactor with a nitrogen gas purge. To neutralize hydrochloric acid, 3.63 mL of triethylamine (TEA) is added, followed by the controlled injection of a solution containing 1.54 mL of acryloyl chloride (ACL) in 40 mL of DCM while the solution is kept in an ice bath. The nitrogen flow is present until all the materials including TEA and ACL are added. After allowing the mixture to react for 24 hours, day two begins with a vacuum distillation, as shown in Figure *3-1* to evaporate the DCM, heating the sealed reactor to

40 degrees Celsius to evaporate the DCM that has a boiling point of 39.6°C. The mixture is then centrifuged for 10 minutes and transferred to a hexane bath to precipitate the polymer. The precipitate is washed three times with hexane to remove any remaining DCM, and the polymer is dried in a vacuum oven for three days. The dried PF68 is then tested using ^{1}H NMR to confirm diacrylation.

Figure 3-1. Setup for the diacrylation of PF68DA

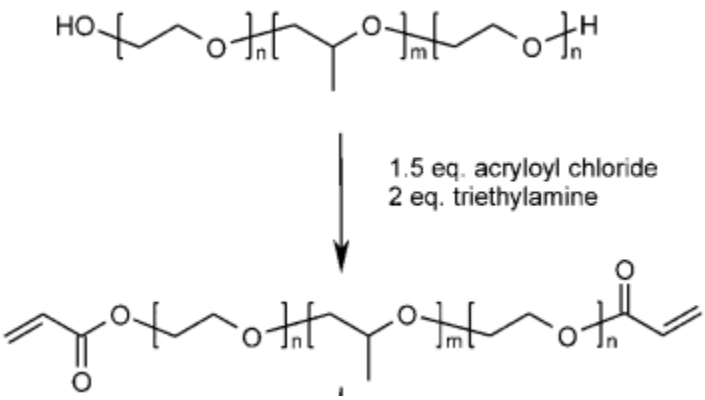

Figure 3-2. General diacrylation scheme for pluronics (35)

3.3 Foaming Method

The hydrogel preparation begins by dissolving PF68DA in water to create a 30 wt.% solution. SDS is added at various concentrations relative to its critical micelle concentration in water (CMC of SDS~8.2 mM): 0 CMC, 0.1 CMC, 1 CMC, 10 CMC, 25 CMC, and 50 CMC.

The SDS concentration is capped at 50 CMC to stay within its solubility limit (approximately 520 mM at 25°C, or 63 CMC). For comparison, a nonporous bulk hydrogel was prepared as a control sample by polymerizing the aqueous solution without foaming, using the same drying conditions as the porous hydrogels to evaluate the effect of porosity on the hydrogel properties. The photoinitiator is added at a concentration of 1 wt.% with respect to the total solution and thoroughly mixed into the solution. Foaming is achieved using a two-syringe method: one syringe contains the prepared solution, while the other is connected to a nitrogen source as described in Zowada et al. (25) .The gas-to-solution ratio (void fraction) is set to 0.5. Nitrogen was preferred over air to prevent oxygen inhibition during UV polymerization. Additionally, gas solubility in water can negatively affect hydrogel formation. CO_2 for instance, has a higher solubility in water compared to N_2 leading to faster coarsening of liquid foams due to Ostwald ripening and consequently larger pore sizes in hydrogel. In addition, if nucleation in the liquid phase is suppressed due to high solubility, bubble formation and embedded porosity becomes limited (9). The syringes are rapidly alternated for 30 seconds, similar to Zowada et al. (25) to generate a uniform foam structure, which is then transferred to a cylindrical mold. Polymerization is initiated by exposing the foam quickly (<10 seconds after foaming) to UV light for 2 minutes and 45 seconds. The UV lamp was a SunRay 600 UV Flood Cure System with a 175 $\frac{mW}{cm^2}$ intensity. The container of the aqueous phase is then sealed with parafilm and left to rest at room temperature for 18 hours. Finally, the hydrogel is dried in a vacuum oven at 25°C for 24-48 hours, resulting in a porous hydrogel structure ready for characterization. The process steps are schematically shown in Figure 3-3.

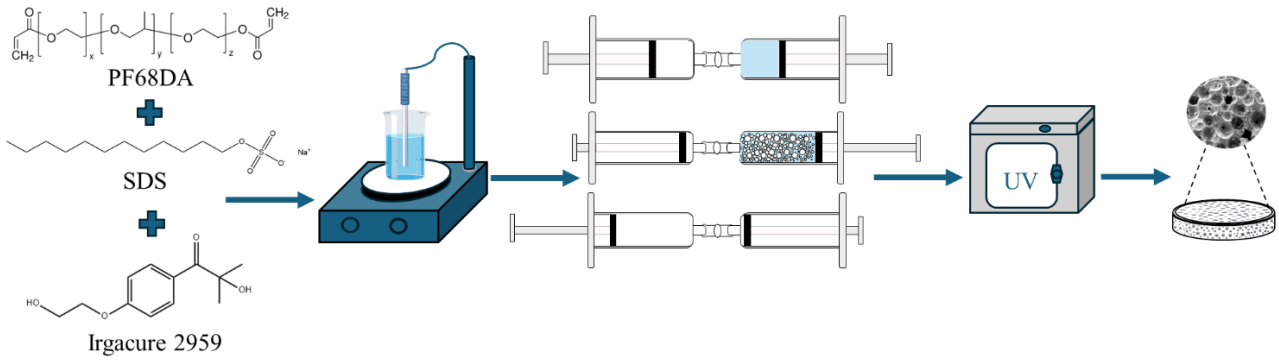

Figure 3-3. Schematic of the polyfoam making process

3.4 Micelles Characterization

A Dynamic Light Scattering (DLS) instrument purchased from Brookhaven Instruments was used to analyze particles and micelle sizes in PF68DA solutions at varying SDS concentrations. A 1 mM PF68DA sample was prepared and tested without any initiator and with different amounts of SDS in the sample. Each run lasted 3 minutes, ensuring accuracy and consistency. The particle size distribution was analyzed based on intensity and volume, providing insights into the size of particles. Measurements were conducted in a cuvette filled to two-thirds of its capacity, optimizing light scattering conditions and ensuring reliable data collection. The measurements were repeated at least 5 times for each concentration of SDS tested.

3.5 Surface Tension Measurement

A tensiometer from Dataphysics, the DCAT 25 model, was employed for measuring the surface tension of PF68DA with various concentrations of SDS at 25 ± 0.5°C. The measurement utilized a Wilhelmy plate (PT 11, Dataphysics) with dimensions of 10 mm in length, 19.9 mm in width, and 0.2 mm in thickness. Measurements were conducted over a period of 1 hour, and each

sample composition was measured in triplicate to ensure the accuracy and reproducibility of results. Prior to each measurement, the Wilhelmy plate was thoroughly washed with acetone and dried using a Bunsen burner to remove any contaminants. For testing, 50 mL of the aqueous sample was transferred into a clean glass vessel for each measurement. To calibrate the instrument, ultrapure deionized water was used before each series of measurements. The surface tension data is then fitted to an equation to determine the equilibrium surface tension. This fitting equation is based on the long-time adsorption approximation of the Ward-Tordai model (36):

$$\gamma(t) = \gamma_{eq} + \frac{nRT\Gamma_{eq}^2}{C}\sqrt{\frac{\pi}{4Dt}} \qquad (1)$$

Where R is the gas constant ($= 8.3145 \frac{\text{J}}{\text{K mol}}$), T is the temperature which value is 298 K (instrument was calibrated to 25 ℃), γ_{eq} is the equilibrium surface tension, $\gamma(t)$ is the surface tension at any time, and C is the bulk concentration. When surface tension results are plotted against $t^{-\frac{1}{2}}$, the intercept gives γ_{eq} while the slope can be used to calculate the diffusion coefficient D.

3.6 Interfacial Dilatational Rheology

An optical tensiometer from Biolin Scientific was used to perform pulsating drop measurements (PD-200 pulsating drop module) on droplets containing 1 mM of PF68DA with varying amounts of SDS for dilatational interfacial rheology tests. In this method, the droplet is generated using a piezoelectric pump connect to a syringe pump setup. As the droplet compresses and expands, the software calculates the sinusoidal changes in the area (A), volume, and surface tension of the droplet over time.

The data were then fitted to calculate the dilatational elastic modulus (E′) and viscous modulus (E′′) using the correlations provided below:

$$|E| = A\frac{d\gamma}{dA} \quad (2)$$

$$E' = |E|cos(\delta) \quad (3)$$

$$E'' = |E|sin(\delta) \quad (4)$$

With δ as the phase angle between the A sinusoidal change and the γ sinusoidal change.

The Gibbs criterion was checked for the samples using the criterion below (37):

$$\frac{d\Delta P}{dR} = 2\frac{(\frac{d\gamma(R)}{R})}{dR} = -\frac{2\gamma}{R^2} + \frac{4E}{R^2} > 0 \rightarrow E - \frac{\gamma}{2} > 0 \quad (5)$$

If this criterion is satisfied, then the bubbles are stable against Ostwald ripening.

3.7 Optical Microscopy

A Nikon Optical Microscope was used to capture clear images of the foam prior to adding the initiator, following the same mixture procedure described earlier. A small volume of the foam was carefully placed on a glass slide, and images were taken within 30 seconds to prevent noticeable coarsening of the foam structure. For enhanced visualization, a DinoCapture camera was connected to the microscope, enabling the acquisition of high-resolution images and videos to monitor the foam stabilization process over time. The captured images were analyzed using ImageJ software, which facilitated the calculation of the diameter of bubbles. Approximately 200 bubbles were used to determine the mean bubble size. All experiments were performed at least three times. The images were captured at different magnifications from $10\times$ and $4\times$.

The different diameters below were used to calculate the polydispersity index (PDI), the mean diameter ($d_{0.5}$) and the Sauter diameter ($D_{[3,2]}$) which is the surface area moment mean diameter using the following equations:

$$d_{0.5} = \frac{\sum d_i}{N} \quad (6)$$

$$D_{[3,2]} = \frac{\sum d_i^3}{\sum d_i^2} \quad (7)$$

$$PDI = \frac{d_{[3,2]}}{d_{0.5}} \quad (8)$$

3.8 Foam Stability Tests

The stability of the foam was quantified by measuring the rate of coalescence at various SDS concentrations to assess the underlying stability mechanisms. For these tests, the aqueous phase was prepared without the initiator to replicate the synthesis procedure accurately. The foam was generated by combining two syringes and mixing the solution for about 30 seconds. The foam height and the volume of the drained liquid phase were recorded continuously using a camera until the foam fully collapsed, which occurred after approximately 2 hours. Images captured of the syringe containing the foam at each time interval were analyzed using ImageJ software to evaluate changes in foam structure and stability over time. The average bubble diameters over time were then modeled using the following power law:

$$D = D_0 + At^n \quad (9)$$

3.9 Scanning Electron Microscopy

After polymerization, the foam samples were frozen in liquid nitrogen in a petri dish and subsequently crushed into smaller fragments to expose their porous structure. The crushed

portions were sputter-coated with a thin layer of gold to enhance conductivity. Imaging was performed using a FEI Quanta microscope. The resulting micrographs were analyzed using ImageJ software to quantify the size of voids and windows. The term window will be used to refer to pore throats in this study. An average of 3 images taken at different areas of the hydrogel at different magnifications were used to ensure statistical reliability. To characterize the number of voids per area ($\overline{N}_v$), number of windows per area ($\overline{N}_w$), and how many windows per void (R_{wv}), the following correlations were used, respectively (25):

$$\overline{N}_v = \frac{\#voids}{A} \quad (10)$$

$$\overline{N}_w = \frac{\#windows}{A} \quad (11)$$

$$R_{wv} = \frac{2\overline{N}_w}{\overline{N}_v} \quad (12)$$

The average degree of openness of the foam ($\overline{O}$) can be calculated using the following correlation:

$$\bar{O} = \frac{(R_{wv} \times D_w^2)}{(4 \times D_v^2)} \quad (13)$$

where the D_w is the window Sauter mean diameter and D_v is the void Sauter mean diameter. As the value of openness approaches zero, it indicates a fully closed-cell foam with minimal window formation. In contrast, higher openness values correspond to open-cell foams with greater interconnectivity and more prominent window structures.

3.10 Mechanical Testing

Mechanical testing was conducted through compression tests using a Discovery Hybrid Rheometer (DHR) equipped with a 20 mm parallel plate geometry. The hydrogel samples,

prepared with a diameter of 20 mm and a thickness of 3 mm, were subjected to an initial compressive load of 0.01 N at a displacement rate of 1 mm/min. Mechanical tests were conducted on hydrogels at both the relaxed and swollen states. This setup allowed for the precise measurement of mechanical properties, including the compressive modulus (K), which reflects the stiffness of the hydrogels under applied stress. The slope in the linear part of stress-strain curve was used to determine K:

$$K = \frac{\sigma}{\varepsilon} = \frac{F/A}{\Delta l/l_0} \quad (14)$$

*w*here σ is the stress, ε is the strain, F is the force, A is the area, l_0 is the original thickness, and Δl is the change in length upon deformation.

3.11 Porosity of samples

The porosity of the hydrogels synthesized from PF68DA and SDS was evaluated by first coating the polymerized samples with a thin hydrophobic layer to prevent water absorption following a process described by Zowada et al (25). This was accomplished by immersing the samples in melted soy wax, creating a uniform barrier. The sealed samples were then placed in a volumetric flask to measure their displacement volume (25) . The actual void fraction (porosity) must be measured by determining the density of the bulk material and polyfoam at different SDS concentrations (ρ_b and ρ). Then the following relation can be used to calculate the void fraction:

$$\Phi_{void} = 1 - \frac{\rho}{\rho_b} \quad (15)$$

3.12 Swelling Kinetics

The dried porous hydrogels were immersed in an ample amount of water to allow for swelling. At specific time intervals, the water was carefully removed using a syringe to ensure accurate measurements, and the hydrogel sample was weighed to determine its swollen weight. After each measurement, fresh water was added to the container to maintain consistent experimental conditions. The water uptake tests were conducted over a total duration of 150 minutes (2 hours and 30 minutes). The water uptake was calculated using the equation provided below, where W_i represents the initial dry weight of the hydrogel, and W_t represents the weight of the hydrogel at time t:

$$Average\ Water\ Uptake = \frac{W_t - W_i}{W_i} \times 100 \quad (16)$$

To normalize the water uptake with porosity, the following equation can be used:

$$Average\ Water\ Uptake^* = (\frac{W_t - W_i}{W_i} \times \Phi_{void}) \times 100 \quad (17)$$

3.13 Surface Sorption

The surface adsorption of hydrogel samples was measured using the Biolin Scientific Optical Tensiometer with the sessile drop (contact angle) option. A drop of about 20 μL was placed on the surface of the hydrogel sample, and adsorption was evaluated by plotting the change in drop volume over time. A high-speed camera captured approximately six frames per second, enabling real-time measurement of surface adsorption for each sample. For reference, the samples were polymerized into cylindrical disks of 20 mm.

3.14 Thermoresponsive Behavior

The thermoresponsive behavior of the hydrogels was evaluated by exposing swollen samples to a temperature range of 5 °C to 60 °C. Samples were first equilibrated at a baseline temperature, such as 25 °C, and then transferred to water baths set at different target temperatures within this range. The water uptake was recorded at various time intervals to analyze the response kinetics at each temperature. To assess the reversibility of this behavior, the samples underwent repeated transitions between two temperatures (e.g., 25 °C and 45 °C) across multiple cycles. This was repeated three times.

4 Results and Discussion

4.1 Surface Tension and Micelle Characterization at the interface

At concentrations below 1 CMC of SDS (~8.2 mM in this study), a mixture of structures was observed, as seen in Table 4-1. The concentration of PF68DA was higher than its CMC (4.4×10^{-4} M), so Pluronic micelles are expected, which can be seen from our results at 0 CMC of SDS (i.e., no SDS present) (38). However, upon adding 0.1 CMC SDS, the copolymer/surfactant complex appeared to suppress copolymer micellization, as the 5 nm peaks disappeared. This trend continues until PF68DA molecules are fully incorporated by SDS. This occurs because SDS strongly binds to PF68DA molecules, forming mixed PF68DA/SDS complexes that exhibit varying surface activity until SDS saturates the interface and begins forming its own micelles at 1 CMC. This observation aligns with findings by Hecht and Hoffmann, who reported that copolymer/surfactant complexes exist only below the CMC of SDS (26,39).

In our study, micelles smaller than 10 nm coexisted with larger aggregates exceeding 100 nm in diameter below the CMC. The typical size of PF68DA micelles (~5 nm), and our observed

aggregate sizes (189 to 228 nm) fall within the range reported in literature (93–320 nm) (38). In our study, a decreasing trend was observed for aggregates, where their sizes decreased with increasing surfactant concentration up to 1 CMC of SDS, likely due to more uniform molecular assembly. Conversely, above the CMC of SDS, micelles disappeared leaving place to larger aggregates as the solution approaches saturation at the interface.

The results suggest that SDS preferentially binds to PPO segments before interacting with PEO chains, influencing micelle formation and aggregate structure (26). Cosgrove et al. described that above the CMC of SDS, the layer thickness of the PEO increases because the micelles along the polymer chain–which is now saturated with surfactant-start to repel each other–causing the polymer to expand into a more stretched out configuration (40). A mechanism for this interaction was proposed in Figure 4-1.

Table 4-1. Summary of micelle and aggregate sizes at varying SDS concentrations, showing the median diameter $d_{0.5}$ and the Sauter diameter ($d_{[3,2]}$) for each structure type.

Structures	**Concentration of SDS**	$\boldsymbol{d_{0.5}}$ $\boldsymbol{(nm)}$	$\boldsymbol{d_{[3,2]}}$ $\boldsymbol{(nm)}$
Micelles	0 CMC	5.3	7.5
	0.1 CMC	4.8	6.9
	1 CMC	4.3	6.3
Aggregates	0 CMC	210.5	221.8
	0.1 CMC	207.7	220.2
	1 CMC	189.7	218.6
	10 CMC	197.9	215.1
	25 CMC	228.9	242.1

Additionally, surface tension measures revealed a progressive decrease over time, confirming that SDS binds strongly to the PF68DA as seen in Figure 4-2A. At very low SDS concentrations, the surface tension remains relatively unchanged, around 40 mN/m in Figure 4-2B. This observation aligns with the explanation by Hecht and Hoffmann, who suggested that at these concentrations, surfactants exist primarily in their monomeric state and compete with the polymer for adsorption at the interface, resulting in minimal changes to surface tension (39).

As the SDS concentration increases, the surfactant begins binding to the hydrophobic PPO block of PF68DA. SDS as a cosurfactant helps form a denser interface to decrease the interfacial tension, especially above the CMC. This trend is clearly depicted in Figure 4-2B, where surface tension decreases progressively with increasing SDS concentration (from 1 CMC to 50 CMC). Additionally, since mixed micelles are present at lower concentrations, one may conclude that the complex of PF68DA and SDS leads to synergistic effects. Notably, the surface tension of SDS alone at 25 CMC was measured at 34.77 mN/m, similar to that of the PF68DA/SDS system at 25 CMC. Therefore, SDS dominates the interface, likely starting at approximately 10 CMC of SDS. Lower surface tension at the air-water interface generally improves foam stability. Based on micelle analysis and surface tension data, 1 CMC serves as a critical transition point, marking significant changes in interfacial stability and micelle formation.

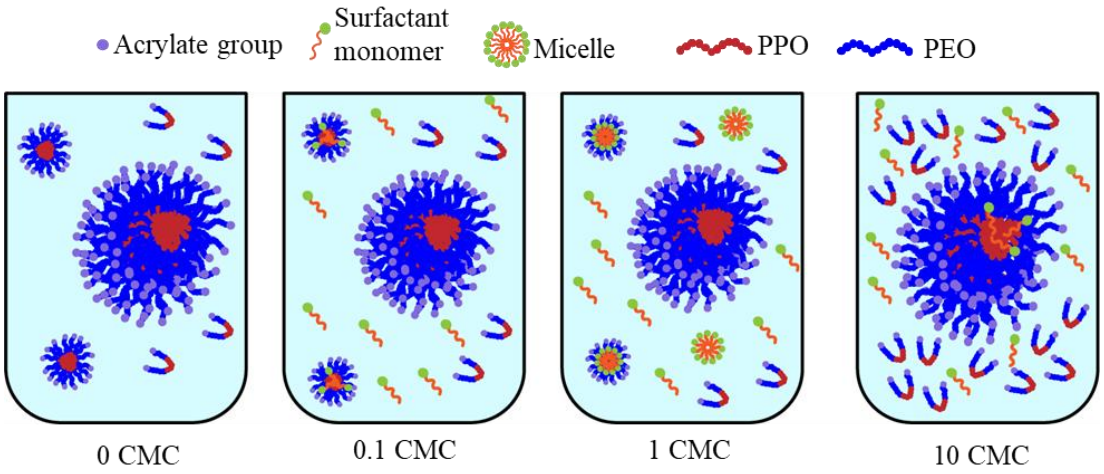

Figure 4-1. Interaction between PF68DA and SDS

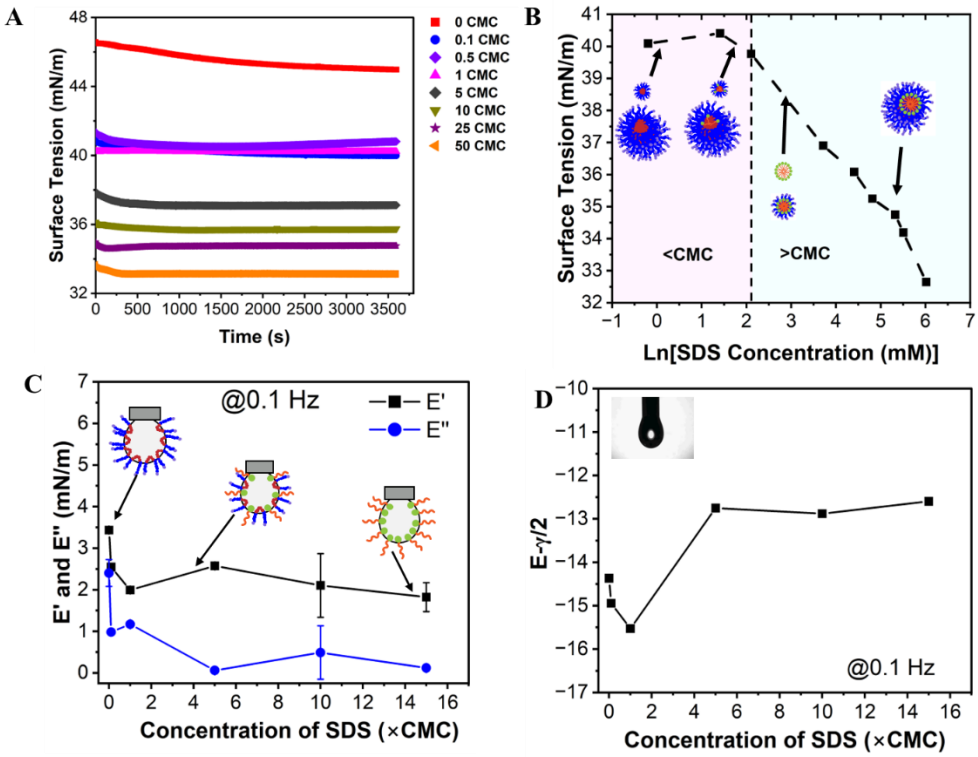

Figure 4-2. (A) Surface tension changes over time for different SDS concentrations, showing a gradual decrease as SDS binds to PF68DA. (B) Surface tension as a function of SDS concentration, highlighting the transition point near the CMC. (C) Elastic modulus (E') and

viscous modulus (E'') as a function of SDS concentration at 0.1 Hz, demonstrating changes in interfacial viscoelasticity. (D) Gibbs criterion ($E - \frac{\gamma}{2}$) plotted against SDS concentration, providing insight into interfacial stability.

4.2 Interfacial Dilatational Rheology Analysis

From the interfacial dilatational rheology analysis in Figure 4-2C, it was observed that as the SDS concentration increases from 0 to just below 1 CMC, E′ initially decreases and E" increases, reaching a minimum in $\tan\delta$ =E"/E′ near 1 CMC. This suggests that as SDS is added, the interfacial film becomes more viscoelastic, potentially due to the interaction between PF68DA and SDS and the different complexes formed. However, once the concentration surpasses the CMC, E′ increases and then reaches a plateaus. The variations observed in E′ and tan δ around 1 CMC may be small enough to fall within the margin of error of the experimental measurements and should therefore be interpreted with caution. Typically, a higher E′ reflects a stronger interfacial film (41). Thus, one may assume that 1 CMC sample has lower stability compared to the rest. However, the reported trend in literature suggests stability peaks near the CMC and then declines at very high SDS concentrations (21,42).

Regarding the Gibbs stability criterion, the plot indicates that the interface is overall unstable against Ostwald ripening, as seen in Figure 4-2D since the values in the y-axis were all negatives. However, the instability decreases above the CMC as the values become less negative, suggesting improved but still limited stability. The Gibbs criterion plateaued at higher SDS concentrations, which may indicate that bubble stability does not improve since the SDS molecules saturate the interface. However, at very high SDS concentrations, bubble destabilization may occur due to depletion attraction forces between bubbles, as reported by

Zhou et al. (38). These inter-bubble forces promote coalescence by reducing the distance between bubbles, even if the film itself remains stable, as demonstrated by Zhou et al (42). These hypotheses will be further evaluated through foam stability tests in the next section.

4.3 Foam analysis

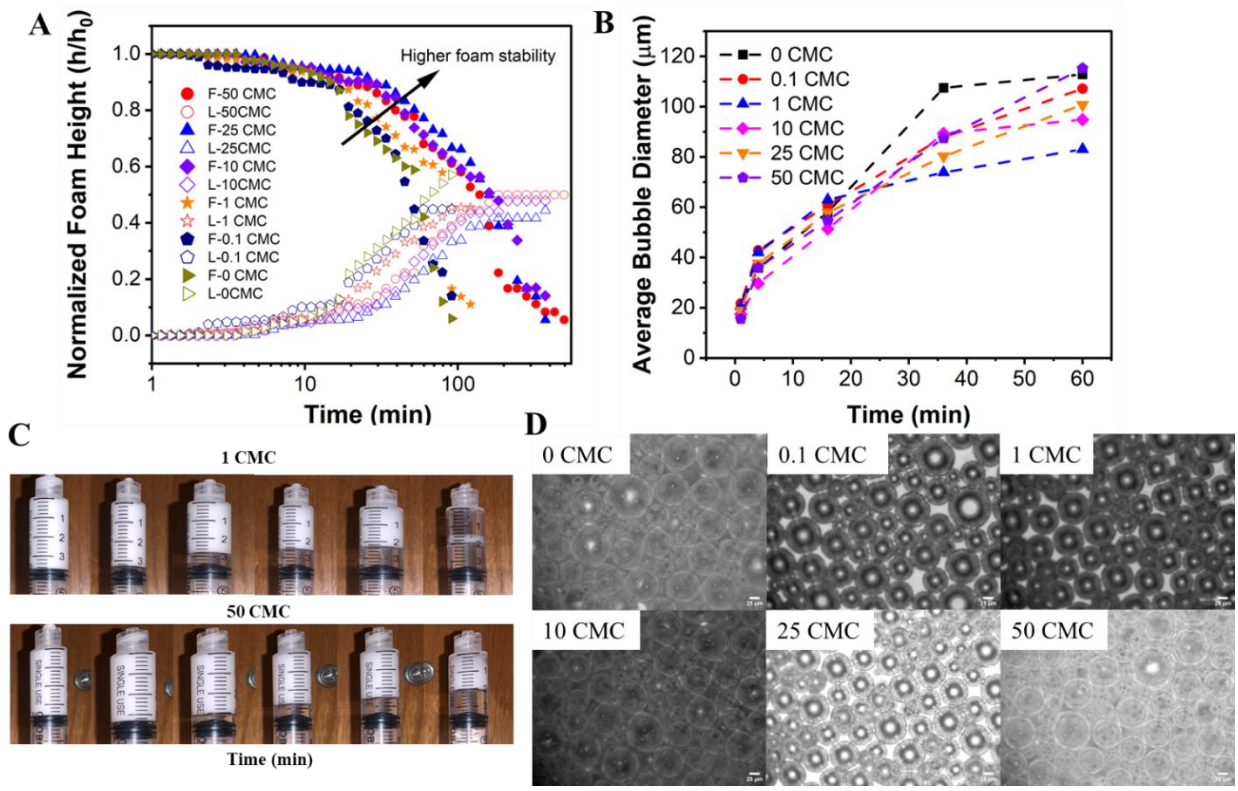

Figure 4-3. (A) Variation of average bubble diameter over time modeled using the power law for different surfactant concentrations. (B) Normalized foam and liquid heights ($\frac{h}{h_0}$) over time for various SDS concentrations, with solid markers (L) representing foam height and empty markers (F) representing liquid height. Higher foam stability is observed at intermediate SDS concentrations, while foam collapse occurs at higher concentrations (e.g., 50 CMC). (C) Time-lapse of foam evolution within syringes at 1 and 50 CMC (left panel). (D) Optical micrographs

of foams at varying SDS concentrations: (a) 0 CMC, (b) 0.1 CMC, (c) 1 CMC, (d) 10 CMC, (e) 25 CMC, and (f) 50 CMC, captured after 12 minutes. Scale bar: 25 μm; magnification: 10×

Table 4-2. Power Law Fitting Parameters for Bubble Diameter Evolution at Various SDS Concentrations

Concentration of SDS ($\times$ CMC)	D_0	A	n	R^2
0	6.15	1.92	0.50	0.96
0.1	13.27	12.21	0.50	0.99
1	0	26.39	0.30	0.97
10	5.49	12.29	0.50	0.97
25	10.51	11.69	0.50	0.99
50	2.45	14.29	0.50	0.99

Considering that the volume fraction used in this study was below 0.74, spherical bubbles were expected, classifying the foams as wet foams, which can be seen in Figure 4-3D. In contrast, dry foams typically exhibit polyhedral structures. The liquid in wet foams is confined at the gas-liquid interface, as observed in the microscopy images in Figure 4-3D. An example of the foam inside the syringe was captured and can be seen in Figure 4-3C for reference.

Foam aging, as described by Zowada et al. (25), primarily involves two well-known mechanisms: coalescence and Ostwald ripening (coarsening), both of which are examined in this study. Ostwald ripening occurs when smaller droplets shrink and larger droplets grow due to pressure-driven diffusion of molecules, while coalescence happens when the thin film between

two adjacent droplets ruptures, allowing them to merge. Based on the exponent of the power law fitting equation, $t^{\frac{1}{2}}$ indicates when coalescence dominates and $t^{\frac{1}{3}}$ when Ostwald ripening is the primary mechanism. The data derived to fit with the power law can be seen in Table 4-2 and in Figure 4-3B. Our findings suggest that the dominant mechanism for bubble size evolution is influenced by surfactant concentration. For concentrations below or above 1 CMC of SDS, coalescence is the primary mechanism. As the system approaches the 1 CMC of SDS and interface becomes more viscoelastic, the rate of coalescence decreases, giving way to Ostwald ripening. However, above the CMC, as SDS concentration increases, the rate of coalescence begins to rise. Between 10 and 25 CMC, bubble size changes minimally, while at 50 CMC, coalescence increases significantly, indicating greater instability due to increased depletion attraction forces (42).

It can be observed that adding SDS generally increases foam stability and slows foam decay up to 25 CMC as seen in Figure 4-3A. However, beyond this point, a negative impact on stability is observed, as stability slightly decreases. At higher CMC values, the aggregates present are relatively unstable and break down, producing more surfactant monomers that can adsorb onto newly formed surfaces. This leads to a faster foam decay at 50 CMC compared to 25 CMC. From all the analysis above, Figure 4-4 was derived to demonstrate the interaction between SDS and PF68DA at the interface and how the depletion attraction increases due to the addition of SDS.

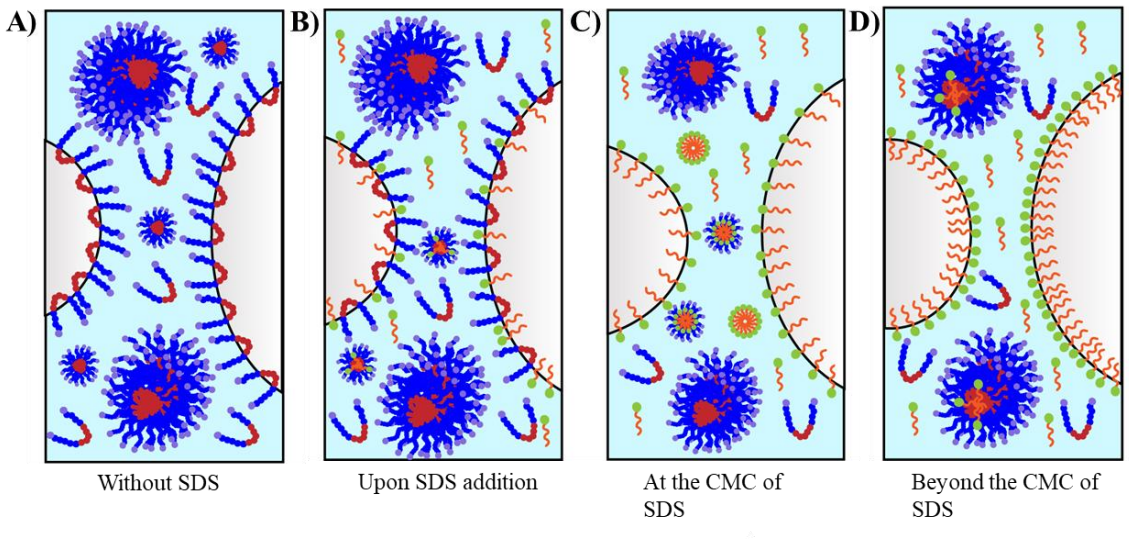

Figure 4-4. Schematic representation of micelle formation in PF68DA/SDS systems at varying SDS concentrations: **(A)** PF68DA above its critical micelle concentration (CMC) forms micelles and aggregates with its unimers present **(B)** As SDS is introduced, mixed micelles of PF68DA and SDS begin to form, leading to a reduction in interfacial tension **(C)** At the CMC the CMC of SDS, there are SDS micelles present and SDS monomers stay at the interface. **(D)** At SDS concentrations well above the CMC, the system becomes saturated with aggregates.

4.4 Morphology Analysis

Figure 4-5 shows the images of the polymerized samples. In this study, we observed that, regardless of the concentration of foaming agents, pore sizes varied, but not significantly, as shown in Table 4-4, where the void diameter decreased from 22 μm to 18 μm. Additionally, the addition of SDS increased the presence of windows (i.e., number of windows per void), with sizes decreasing from 5.7 μm to 3.4 μm. As explained in the previous section, the formation of more windows of smaller sizes is due to the increased depletion attraction forces, induced by higher and/or larger PF68DA aggregates in bulk since SDS replaces PF68DA at the interface (42). The trends in openness and the number of windows per void are different than those reported in HIPE

systems (42). In other words, increasing the concentration of SDS allows for the formation of thinner liquid films between the bubbles that are more likely to break, allowing for the formation of more windows per void in the structure with a higher openness. Both the window frequency and openness increase with SDS concentration and remain relatively constant between 10-25 CMC. This trend correlates with the increase in E′ observed in interfacial rheology but should not be interpreted as a direct relationship, as the trends are not perfectly aligned. Similarly, while Gibbs stability improves around the CMC, it is not directly predictive of window formation. Increased SDS concentration led to greater pore interconnectivity, though this does not necessarily imply an increase in total porosity.

As discussed in section 2.3, foam templating presents the challenge of maintaining structural integrity after polymerization. Here, we successfully demonstrated that the bubble size observed during foam formation was consistent with the pore size after polymerization, ensuring structural stability as seen in Table 4-3.Only at 50 CMC, the presence of instability during the polymerization process was reflected in the increase of diameter from bubble to void. At 50 CMC, spontaneous self-assembly processes can occur in bulk solutions, forming higher molecular structural aggregates from lower molecular weight pre-micellar species. This phenomenon could explain the formation of irregular, "clumpy" bulk structures within the hydrogel matrix, as observed at 50 CMC in Figure 4-5F.

Table 4-3. Comparison of the Bubble Size before Polymerization and the Void Size after Polymerization

C_{SDS} ($\times CMC$)	**Average bubble diameter < 1 min (µm)**	**Average void diameter (µm)**
0	20.9	22.4
0.1	21.7	23.2
1	20.5	20.1
10	17.4	18.9
25	18.9	18.5
50	15.6	20.0

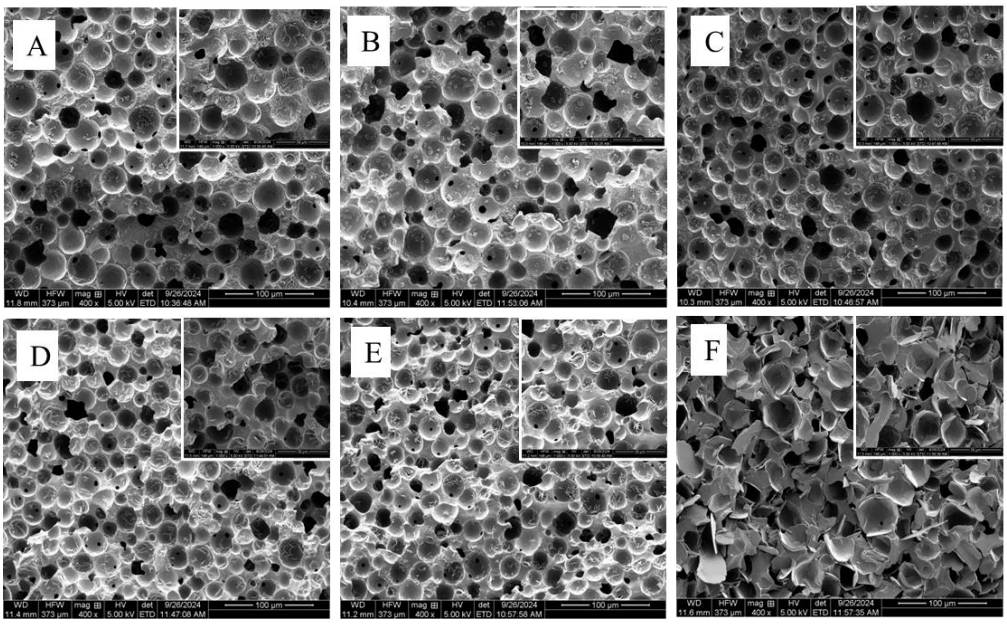

Figure 4-5. SEM micrographs of hydrogel foams with varying SDS concentrations at two magnifications: (A) 0 CMC, (B) 0.1 CMC, (C) 1 CMC, (D) 10 CMC, (E) 25 CMC, and (F) 50

CMC. The main images were taken at 400× magnification with a scale bar of 100 µm, while the insets were taken at 1000× magnification with a scale bar of 50 µm, highlighting structural variations across SDS concentrations

Table 4-4. Summary of void and window size distributions, pore size characterization parameters, and interconnectivity metrics for hydrogels at varying SDS concentrations (× CMC).

Concentration of SDS (× $\boldsymbol{CMC}$**)**	**Void**				**Window**				**Interconnectivity**	
	$\boldsymbol{D_{0.5}}$ $(\boldsymbol{\mu m})$	$\boldsymbol{D_{[3,2]}}$ $(\boldsymbol{\mu m})$	**PDI**	$\boldsymbol{\bar{N}_v \times 10^3}$ $(\frac{\boldsymbol{voids}}{\boldsymbol{mm^2}})$	$\boldsymbol{D_{0.5}}$ $(\boldsymbol{\mu m})$	$\boldsymbol{D_{[3,2]}}$ $(\boldsymbol{\mu m})$	**PDI**	$\boldsymbol{\bar{N}_w \times 10^3}$ $(\frac{\boldsymbol{windows}}{\boldsymbol{mm^2}})$	$\boldsymbol{R_{wv}}$	$\boldsymbol{\bar{O}}$
0	22.3	25.7	1.15	1.50	4.7	5.2	1.09	0.10	0.1	0.0013
0.1	23.2	26.9	1.16	1.52	4.5	5.2	1.11	0.15	0.2	0.0018
1	20.1	23.4	1.17	1.93	3.6	4.1	1.13	0.30	0.3	0.0019
10	18.8	21.4	1.14	2.21	3.6	3.9	1.10	0.34	0.3	0.0027
25	18.5	20.9	1.14	2.27	3.4	3.8	1.13	0.36	0.3	0.0027

4.5 Swelling Kinetics

High SDS concentrations enhanced the swelling and speeded water uptake of hydrogels up to 25 CMC in Figure 4-6B and Figure 4-6C. The hydrogel increased in diameter by about 2×, corresponding to an estimated 8-fold increase in volume after swelling as seen in Figure 4-6A. The normalized water uptake in Figure 4-6C is the swelling capacity multiplied by the actual porosity of the sample as instability can occur during the crosslinking process. The measured porosity of the samples was lower than the theoretical void fraction, revealing a 50% reduction in

water uptake for all the samples. The porosity, which will be seen in Table 4-5, shows an increase with higher SDS concentrations, indicating stronger capillary forces and consequently greater water uptake. This trend is also linked to smaller voids and window sizes as SDS concentration increases.

At 50 CMC, SDS started leaching out of the polyfoam. In other words, while adding SDS improves swelling, an optimal concentration was achieved at 10-25 CMC. Beyond this point, swelling kinetics decreased as SDS leached into the water. Conductivity measurements confirmed that 8.57 mM of SDS leached out, close to its CMC, resulting in micelle formation in the water matrix as seen in Figure 4-7. At 50 CMC, although the polyfoam showed the highest average water uptake, the irregular pore morphology and decreased stability—likely due to SDS leaching—may have affected the structural integrity and long-term swelling behavior. These findings suggest that 25 CMC is the optimal SDS concentration for balanced swelling and stability (25).

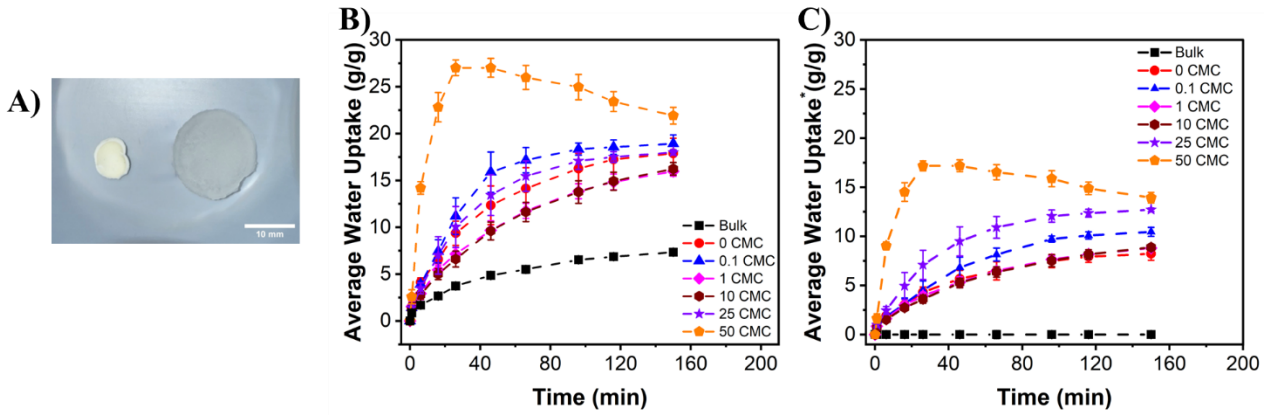

Figure 4-6. (A) Dry hydrogel (left) and swollen hydrogel after 150 minutes (right) (B) Average water uptake ratio of porous hydrogels foams over 2 h and 20 min at 25 C. (C) Average normalized water uptake ratio ($\bar{W}$*) of porous hydrogels over 2 h and 20 min where the water uptake is multiplied by the measured porosity of the material.

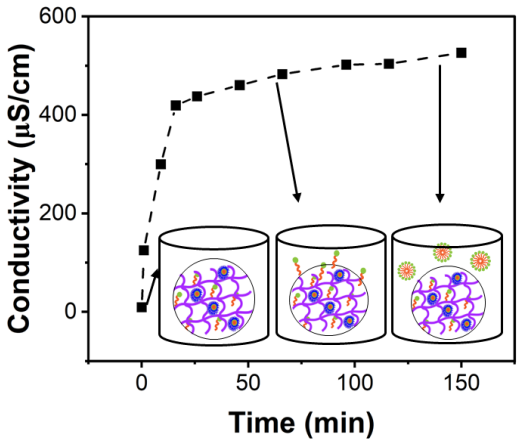

Figure 4-7. Conductivity over time for water containing 50 CMC of SDS, demonstrating the thermoresponsive behavior of the system. Calibration plots used to calculate the SDS concentration in the water are provided in the appendix in 6.1.

4.6 Thermoresponsive behavior of hydrogels

From the results in Figure 4-8A and Figure 4-8 B, it was found that adding surfactants enhances the thermoresponsive behavior of the hydrogel. Foaming in general was also proven to improve the reversibility of the thermoresponsive behavior when comparing the bulk sample to the 0 CMC one in Figure 4-8B. Lee et al. reported that the presence of bound surfactants within a gel network increases the volume phase transition temperature (VPTT) and swelling ability due to heightened electrostatic repulsion arising from the bound surfactant aggregates as we have seen at high SDS concentrations (43). The VPTT is a critical parameter, as it defines the temperature at which a polymer undergoes drastic swelling or deswelling. Based on the results shown in Figure *4-8*A, the VPTT for the hydrogel without surfactants (0 CMC) is approximately 10°C. As SDS concentration increases to 10 and 25 CMC, the swelling peak shifts to around 35 °C, suggesting an increase in the VPTT. However, at 50 CMC, the trend becomes less distinct, and the apparent VPTT may decrease again or become more difficult to interpret due to

irregular swelling behavior. These observations indicate that SDS concentration influences the thermal response of the hydrogel network, although the response at higher concentrations (e.g., 50 CMC) may be impacted by structural instability. This shift indicates that the inclusion of SDS influences the hydrogel's response to temperature changes. Surfactants interact with the hydrogel's polymer network, modifying the balance between hydrophilic and hydrophobic interactions. Adding an anionic surfactant like SDS introduces negatively charged species into the hydrogel as discussed in previous results. These species interact with the polymer chains and water molecules, enhancing the hydrophilicity of the network while disrupting some hydrophobic interactions. Consequently, water absorption is improved as seen in the swelling tests results.

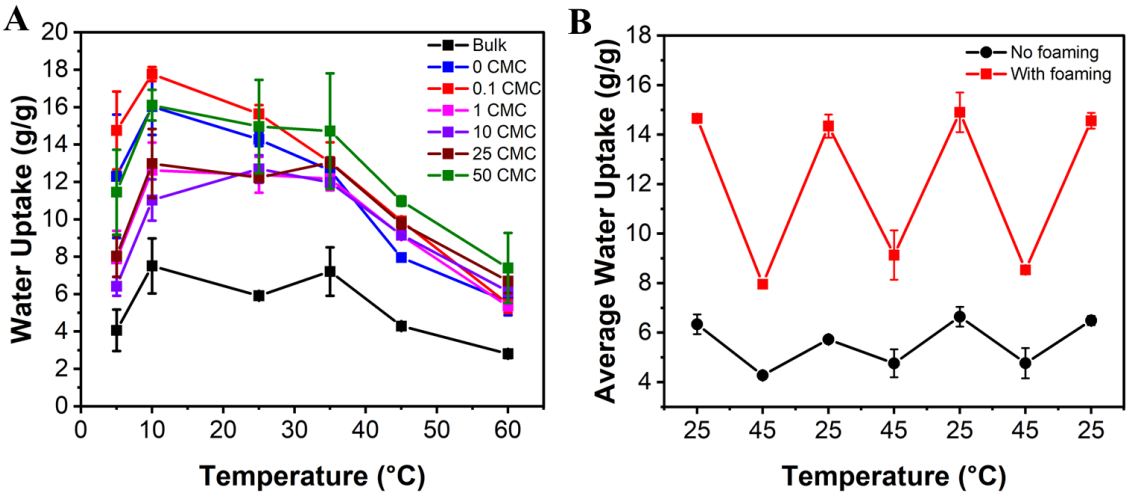

Figure 4-8. Thermoresponsive behavior of porous hydrogels at temperatures ranging from 5°C to 60°C

4.7 Surface Adsorption

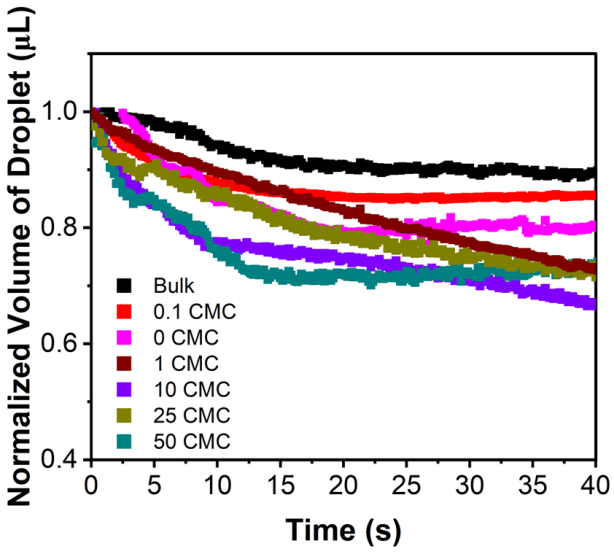

Figure 4-9. Real-time surface absorption in 30 s by contact angle of porous hydrogel samples with different concentrations of SDS

As seen in Figure 4-9, real-time surface sorption was evaluated by tracking the change in droplet volume for 30 seconds on porous hydrogel samples containing different concentrations of SDS. The results show that the bulk sample, with no SDS, retained nearly all of its droplet volume throughout the measurement period, indicating minimal surface absorption and low wettability. In contrast, porous samples exhibited progressively greater droplet volume loss as SDS concentration increased, reflecting enhanced surface sorption. Notably, the 50 CMC sample demonstrated the most rapid decline in droplet volume, followed by the 25 CMC and 10 CMC samples. These trends indicated that higher SDS concentrations improved surface wettability and promoted faster water spreading or absorption. 10 CMC sample, however, showed the most consistent decrease over time.

4.8 Mechanical testing

The mechanical strength of the hydrogels was found to be significantly influenced by the concentration of SDS, as seen in Figure 4-10 and Table 4-5. As SDS concentration increased, a reduction in Young's modulus was observed, indicating a softer and less rigid material. While higher SDS concentrations led to greater pore interconnectivity, as reflected in the openness values, it is important to note that interconnectivity does not necessarily correlate with overall porosity.

The bulk sample, which lacked SDS and foaming, exhibited the highest modulus due to its denser, non-porous structure. Samples below CMC of SDS had a higher K value at the relaxed state (i.e., as-synthesized state) compared to the ones above CMC. K in the relaxed state sharply decreases with increasing SDS concentration, reaching a minimum at 10 CMC. Surprisingly, at 25 CMC, there is a slight increase in modulus (0.87 kPa), followed by a larger increase at 50 CMC (2.34 kPa). At 50 CMC, the increase in the modulus was due to excessive SDS leaching into the surrounding water over time, leaving the structure with less surfactants and a denser network. In the swollen state, the modulus values for SDS-based hydrogels are lower across the board (0.39–0.92 kPa) compared to the bulk sample (2.38 kPa). Additionally, at 50 CMC, as SDS leaches out, it further weakens the structure following the swelling, especially in the swollen state, where we observed the lowest E value.

When comparing relaxed and swollen states, the modulus was consistently lower in the swollen samples, reflecting the weakening effect of water uptake on the hydrogel network. This trend aligns with the role of SDS in enhancing swelling and porosity but highlights a trade-off between increased water sorption and reduced mechanical stability.

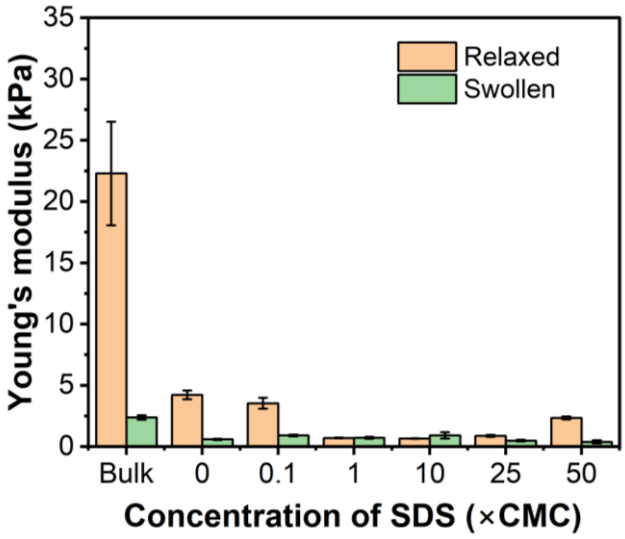

Figure 4-10. Comparison of Young's modulus for polyfoam hydrogels in both relaxed and swollen states at varying SDS concentration. The bulk sample exhibited the highest modulus, while samples with higher SDS concentrations showed reduced mechanical strength due to increased porosity and SDS leaching.

Table 4-5. Void Fraction of Polyfoam Hydrogels at Various SDS Concentrations

Concentration of SDS ($\times CMC$)	Density (g/mL)	ϕ_{void}	E Relaxed state (kPa)	E Swollen State (kPa)
Bulk	1.10	-	22.29 $\pm$4.23	2.382 $\pm$0.19
0	0.59	0.46	4.22 $\pm$0.35	0.59$\pm$0.06
0.1	0.52	0.53	3.53 $\pm$0.44	0.91$\pm$0.07
1	0.49	0.55	0.71 $\pm$0.03	0.72$\pm$0.07
10	0.50	0.54	0.66 $\pm$0.03	0.92$\pm$0.26
25	0.32	0.70	0.87$\pm$0.08	0.49$\pm$0.07
50	0.40	0.64	2.34 $\pm$0.13	0.39$\pm$0.13

5 Final Comments and Future Work

5.1 Summary of Findings

This research explores the fabrication of foam-templated porous hydrogels using a nitrogen gas foaming method with a dual-syringe setup connected by a Luer lock. The goal was to tune hydrogel structure, swelling behavior, and thermoresponsiveness. By leveraging interactions between the block copolymer PF68DA and the co-surfactant SDS, we developed a cost-effective synthesis approach that enabled control over morphology and porosity. A key finding is that increasing SDS concentration significantly influenced micelle formation and interfacial properties of the solution prior to crosslinking, which in turn affected foam stability. Below the CMC, mixed micelles formed through surfactant-copolymer interactions. Above the CMC, intensified depletion attraction forces destabilized the foam by reducing the size of the interfacial film, resulting in more window formation and smaller pores in the polyfoam structure. At very high concentrations (50 CMC), SDS leaching further weakened the structure and causes a reduction in the swelling capacity, though it slightly increased mechanical strength in the swollen state as the polyfoam now had less surfactant.

Surface tension and dilatational interfacial rheology confirmed SDS's critical role in modifying interfacial activity and micelle dynamics. At 25 CMC, the surface tension and elastic modulus remained unchanged with or without PF68DA. With PF68DA, the elastic modulus initially declined as SDS increased up to the CMC, then it increased above the CMC, but later plateaued, suggesting saturation at the interface and altered film strength. Foam stability studies showed that dual surfactant systems extended foam lifespan and prevented coalescence. Intermediate SDS concentrations (10-25 CMC) supported long-lasting foam and uniform pore

formation after polymerization. In contrast, concentrations above 50 CMC led to rapid foam breakdown due to excess surfactant accumulation and aggregate formation, resulting in irregular structures in the polyfoam. SEM imaging confirmed that SDS concentration directly influenced void and window sizes: voids averaged ~20 μm and windows ~5 μm. At high SDS concentrations, excessive micelle aggregation led to some loss of stability before gelation and a non-uniform structure after curing.

Swelling kinetics revealed that foam-templated hydrogels absorbed water more rapidly than non-porous ones. SDS enhanced this behavior, with peak water uptake at 25 CMC. Beyond this point, leaching reduced swelling efficiency. Thermoresponsiveness also improved with SDS, showing a shift in volume phase transition temperature (VPTT), with optimal response at 25 CMC and 35°C. Higher concentrations negatively affected the thermal response with a response at about 10 °C due to excess surfactant. Mechanical testing showed that increased porosity led to reduced Young's modulus. Bulk hydrogels were stiffer due to their dense structure, while porous hydrogels at 10-25 CMC offered a better trade-off between improved stability, good swelling, and good thermal response even with the lower mechanical properties.

Overall, this study demonstrates that carefully tuning SDS concentration and foam stability during polymerization allows for the design of porous hydrogels with customizable properties. These findings enhance the understanding of surfactant-polymer interactions and offer new pathways for developing functional materials in biomedical and environmental applications

5.2 Contributions to the Field

This research advances the field of foam-templated porous hydrogels by providing new insights into how surfactant-polymer interactions influence structure, stability, swelling behavior,

and thermoresponsiveness. It also introduces a novel cost-effective surfactant-based approach for producing polyfoams without the need for additional chemical crosslinkers, which are commonly used in conventional methods. First, this study provides a detailed analysis of how SDS interacts with PF68DA at varying concentrations and how cosurfactants modify micelle formation, surface tension, and interfacial dynamics, which are essential for designing stable foam-based hydrogel systems. This research demonstrates how cosurfactant concentration impacts foam stability during before and after crosslinking. We successfully achieved high swelling with moderate mechanical strength, addressing a challenge in the field of polyfoam hydrogels. Additionally, we achieved void sizes significantly smaller than 100 μm, reaching 20 μm, which, compared to other available polyfoams, has been very hard to achieve. The study establishes an optimal SDS concentration range, both below the CMC (0.1-1 CMC) and above the CMC (10-25 CMC), for achieving stable, uniform pore structures in hydrogel foams, addressing a key challenge in porous hydrogel fabrication. No washing of the hydrogel is necessary up to 50 CMC; however, at this concentration, washing may be important to remove excess surfactant.

By tuning SDS concentration, this work successfully explores pore size and interconnectivity, enabling improved water uptake and swelling behavior. The ability to control these structural properties is crucial for applications in drug delivery, wound healing, and, more specifically, the application of interest, space exploration. This study presents a scalable, cost-effective approach for fabricating porous hydrogels using a UV-initiated polymerization technique. By eliminating additional chemical crosslinkers and leveraging PF68DA as both a surfactant and copolymer precursor, this method reduces the need for complex synthesis steps, making it more sustainable and industrially viable.

These contributions pave the way for further exploration of foam-based hydrogel systems in both academic research and commercial applications, especially for my future Ph. D research.

5.3 Suggestions for Future Research

While this study provides valuable insights into foam-templated porous hydrogels, several key areas remain open for further investigation. Future research should focus on the long-term stability of these porous hydrogels, particularly in real-world environments. Investigating how hydrogel porosity, mechanical integrity, and swelling capacity change over time will be crucial for applications in biomedical and environmental engineering. While SDS was used as a model surfactant, exploring other surfactant systems (e.g., cationic or other anionic surfactants) could provide new insights into how different molecular interactions affect foam stability and hydrogel performance. Additionally, testing different triblock copolymers beyond PF68DA could expand the material's versatility. Incorporating nanoparticles (e.g., silica, graphene oxide, or cellulose nanocrystals) into the hydrogel matrix could improve foam stability, mechanical strength, conductivity, and thermal stability. Given the increasing emphasis on sustainable materials, evaluating the biodegradability and environmental footprint of these hydrogels is an important next step.

Investigating how biodegradable surfactants or green foaming agents influence hydrogel properties could support the development of eco-friendly biomaterials. While SEM was used to characterize hydrogel porosity, 3D imaging techniques such as X-ray microtomography or cryo-SEM could provide a more detailed understanding of pore connectivity, distribution, and structure-property relationships. Expanding beyond thermoresponsive behavior, future work could explore multi-functional hydrogels that respond to pH for example, enabling next-

generation smart materials. By addressing these research gaps, the field of foam-templated porous hydrogels can continue to evolve, unlocking new possibilities for various applications.

5.4 References

1. Annabi N, Nichol JW, Zhong X, Ji C, Koshy S, Khademhosseini A, et al. Controlling the Porosity and Microarchitecture of Hydrogels for Tissue Engineering [Internet]. 2010. Available from: www.liebertpub.com
2. Lundin JG, Daniels GC, McGann CL, Stanbro J, Watters C, Stockelman M, et al. Multi-Functional Polyurethane Hydrogel Foams with Tunable Mechanical Properties for Wound Dressing Applications. Macromol Mater Eng. 2017 Mar 1;302(3).
3. Dehli F, Rebers L, Stubenrauch C, Southan A. Highly Ordered Gelatin Methacryloyl Hydrogel Foams with Tunable Pore Size. Biomacromolecules. 2019 Jul 8;20(7):2666–74.
4. Mitura S, Sionkowska A, Jaiswal A. Biopolymers for hydrogels in cosmetics: review. Vol. 31, Journal of Materials Science: Materials in Medicine. Springer; 2020.
5. Chen J, Park K. Synthesis of fast-swelling, superporous sucrose hydrogels [Internet]. Available from: www.elsevier.com/locate/carbpol
6. Li N, Luo L, Guo C, He J, Wang S, Yu L, et al. Shape-controlled fabrication of cost-effective, scalable and anti-biofouling hydrogel foams for solar-powered clean water production. Chemical Engineering Journal. 2022 Mar 1;431.
7. Teng Z, Luo Y, Pearlstein DJ, Zhou B, Johnson CM, Mowery J, et al. Agarose hydrogel composite supports microgreen cultivation with enhanced porosity and continuous water supply under terrestrial and microgravitational conditions. Int J Biol Macromol. 2022 Nov 1;220:135–46.

8. Djemaa I Ben, Auguste S, Drenckhan-Andreatta W, Andrieux S. Hydrogel foams from liquid foam templates: Properties and optimisation. Adv Colloid Interface Sci. 2021 Aug 1;294:102478.

9. Foudazi R, Zowada R, Manas-Zloczower I, Feke DL. Porous Hydrogels: Present Challenges and Future Opportunities. Vol. 39, Langmuir. American Chemical Society; 2023. p. 2092–111.

10. Andrieux S, Quell A, Stubenrauch C, Drenckhan W. Liquid foam templating – A route to tailor-made polymer foams. Vol. 256, Advances in Colloid and Interface Science. Elsevier B.V.; 2018. p. 276–90.

11. Serhan M, Sprowls M, Jackemeyer D, Long M, Perez ID, Maret W, et al. Total iron measurement in human serum with a smartphone. In: AIChE Annual Meeting, Conference Proceedings. American Institute of Chemical Engineers; 2019.

12. Graeber G, Díaz-Marín CD, Gaugler LC, El Fil B. Intrinsic Water Transport in Moisture-Capturing Hydrogels. Nano Lett. 2024 Apr 3;24(13):3858–65.

13. Guo Y, de Vasconcelos LS, Manohar N, Geng J, Johnston KP, Yu G. Highly Elastic Interconnected Porous Hydrogels through Self-Assembled Templating for Solar Water Purification. Angewandte Chemie - International Edition. 2022 Jan 17;61(3).

14. Choudhary H, Raghavan SR. Superfast-Expanding Porous Hydrogels: Pushing New Frontiers in Converting Chemical Potential into Useful Mechanical Work. ACS Appl Mater Interfaces. 2022 Mar 23;14(11):13733–42.

15. Zhou Y, Cui M, Liao S, Yuan B, Shi R, Hu X, et al. An injectable macroporous hydrogel templated by gasification reaction for enhanced tissue regeneration. Supramolecular Materials. 2023 Dec 1;2.

16. Staruch RMT, Glass GE, Rickard R, Hettiaratchy SP, Butler PEM. Injectable Pore-Forming Hydrogel Scaffolds for Complex Wound Tissue Engineering: Designing and Controlling Their Porosity and Mechanical Properties. Vol. 23, Tissue Engineering - Part B: Reviews. Mary Ann Liebert Inc.; 2017. p. 183–98.
17. Chen ZX, Zha XJ, Xia YK, Ling TX, Xiong J, Huang JG. 3D Foaming Printing Biomimetic Hierarchically Macro-Micronanoporous Hydrogels for Enhancing Cell Growth and Proliferation. ACS Appl Mater Interfaces. 2024 Feb 28;16(8):10813–21.
18. Feng L, Hao Y, Zhu M, Zhai Y, Yang L, Liu Y, et al. Incorporation of Laminarin-Based Hydrogel with Graphene Foam to Enhance the Toughness of Scaffold and Regulate the Stem Cell Behavior. ACS Biomater Sci Eng. 2019 Oct 14;5(10):5295–304.
19. Abed FN, Abdelhedi M. Synthesis of a Hydrogel Polymer Using Sodium Lauryl Ether Sulphate as a Surfactant and Its Application in Agricultural. Chemical Methodologies. 2024 Dec 1;8(12):874–91.
20. Abd-Elsalam KA, Hashim AF, Ahmed FK, Thomas S. Nanotechnology in the Life Sciences Biopolymeric Nanoparticles for Agricultural Applications.
21. Pinthong T, Yooyod M, Mahasaranon S, Viyoch J, Jongjitwimol J, Ross S, et al. Designing Stable Macroporous Hydrogels: Effects of Single and Dual Surfactant Systems on Porous Architecture, Absorption Capacity, and Mechanical Strength. ACS Appl Polym Mater. 2025;
22. Zhang H, Yu Y, Li Y, Lin L, Zhang C, Zhang W, et al. A novel BC/g-C3N4 porous hydrogel carrier used in intimately coupled photocatalysis and biodegradation system for efficient removal of tetracycline hydrochloride in water. Chemosphere. 2023 Mar 1;317.

23. Getachew BA, Kim SR, Kim JH. Self-healing hydrogel pore-filled water filtration membranes. Environ Sci Technol. 2017 Jan 17;51(2):905–13.

24. Guo Y, Bae J, Fang Z, Li P, Zhao F, Yu G. Hydrogels and Hydrogel-Derived Materials for Energy and Water Sustainability. Vol. 120, Chemical Reviews. American Chemical Society; 2020. p. 7642–707.

25. Zowada R, Foudazi R. Polyfoam: Foam-Templated Microcellular Polymers. Langmuir. 2020 Jul 14;36(27):7868–78.

26. Sastry N V., Hoffmann H. Interaction of amphiphilic block copolymer micelles with surfactants. In: Colloids and Surfaces A: Physicochemical and Engineering Aspects. Elsevier B.V.; 2004. p. 247–61.

27. Dehli F, Southan A, Drenckhan W, Stubenrauch C. Tailoring and visualising pore openings in gelatin-based hydrogel foams. J Colloid Interface Sci. 2021 Apr 15;588:326–35.

28. Shi XN, Wang WB, Wang AQ. Effect of surfactant on porosity and swelling behaviors of guar gum-g-poly(sodium acrylate-co-styrene)/attapulgite superabsorbent hydrogels. Colloids Surf B Biointerfaces. 2011 Nov 1;88(1):279–86.

29. Antonietti M, Caruso RA, Göltner CG, Weissenberger MC. Morphology Variation of Porous Polymer Gels by Polymerization in Lyotropic Surfactant Phases. Macromolecules. 1999 Mar 9;32(5):1383–9.

30. Ghosh A, Orasugh JT, Ray SS, Chattopadhayay D. Foaming Technology. In: ACS Symposium Series. American Chemical Society; 2023. p. 1–27.

31. Jin FL, Zhao M, Park M, Park SJ. Recent trends of foaming in polymer processing: A review. Vol. 11, Polymers. MDPI AG; 2019.

32. Tan H, Tu S, Zhao Y, Wang H, Du Q. A simple and environment-friendly approach for synthesizing macroporous polymers from aqueous foams. J Colloid Interface Sci. 2018 Jan 1;509:209–18.

33. Zhang Z, Tan H, Zhao Y, Wang Q, Wang H. Facile synthesis of macroporous zwitterionic hydrogels templated from graphene oxide-stabilized aqueous foams. J Colloid Interface Sci. 2019 Oct 1;553:40–9.

34. Saadat Y, Tabatabaei SM, Kim K, Foudazi R. Thermoresponsive antifouling ultrafiltration membranes from mesophase templating. J Memb Sci. 2023 Oct 15;684.

35. Cellesi F, Tirelli N, Hubbell JA. Materials for cell encapsulation via a new tandem approach combining reverse thermal gelation and covalent crosslinking. Macromol Chem Phys. 2002 Jul 29;203(10–11):1466–72.

36. Nele M. An analytically solvable numerical approximation to Ward-Tordai equation applied to Langmuir adsorption. Colloids Surf A Physicochem Eng Asp. 2022 Sep 5;648.

37. Fyrillas MM, Kloek W, Van Vliet T, Mellema J. Factors determining the stability of a gas cell in an elastic medium. Langmuir. 2000 Feb 8;16(3):1014–9.

38. Olea AF, Carrasco H, Espinoza L, Acevedo B. SOLUBILIZATION OF P-ALKYLPHENOLS IN PLURONICS F-68 AND F-127 MICELLES: PARTITION COEFFICIENTS AND EFFECT OF SOLUTE ON THE AGGREGATE STRUCTURE. Vol. 59, J. Chil. Chem. Soc. 2014.

39. Hecht E, Hoffmann H. Interaction of ABA Block Copolymers with Ionic Surfactants in Aqueous Solution The binding of SDS on F127 begins at concentration far below the critical micelle concentration of SDS [Internet]. Vol. 10, Langmuir. 1994. Available from: https://pubs.acs.org/sharingguidelines

40. Cosgrove T, Mears SJ, Obey T, Thompson L, Wesley RD. Polymer, particle, surfactant interactions. Vol. 149, Colloids and Surfaces A: Physicochemical and Engineering Aspects. 1999.

41. Jin Y, Liu D, Hu J. Effect of surfactant molecular structure on emulsion stability investigated by interfacial dilatational rheology. Polymers (Basel). 2021 Apr 1;13(7).

42. Zhou M, Foudazi R. Effect of Cosurfactant on Structure and Properties of Polymerized High Internal Phase Emulsions (PolyHIPEs). Langmuir. 2021 Jul 6;37(26):7907–18.

43. Lee CH, Bae YC. Effect of surfactants on the swelling behaviors of thermosensitive hydrogels: applicability of the generalized Langmuir isotherm. RSC Adv [Internet]. 2016 Oct 28 [cited 2025 Jan 6];6(105):103811–21. Available from: https://pubs.rsc.org/en/content/articlehtml/2016/ra/c6ra19696a

6 Appendix

6.1 Additional Data and Figures

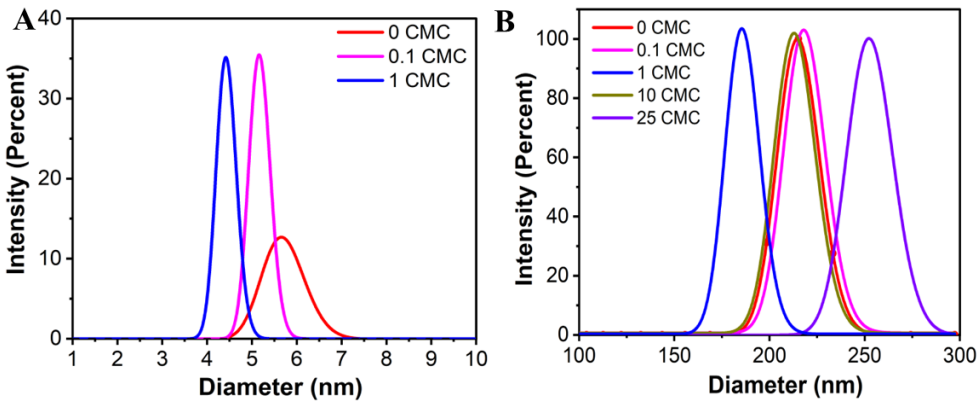

Figure 6-1. Micelle size distribution in 1 mM PF68DA with varying SDS concentrations below and above the CMC of SDS. (A) Micelle size distribution in the region below 1 CMC, where

micelles with diameters less than 10 nm are observed. (B) Larger aggregate distribution across concentrations, showing aggregates present both below and above the CMC. The transition from smaller micelles to larger aggregates highlights the effect of SDS concentration on micelle and aggregate formation.

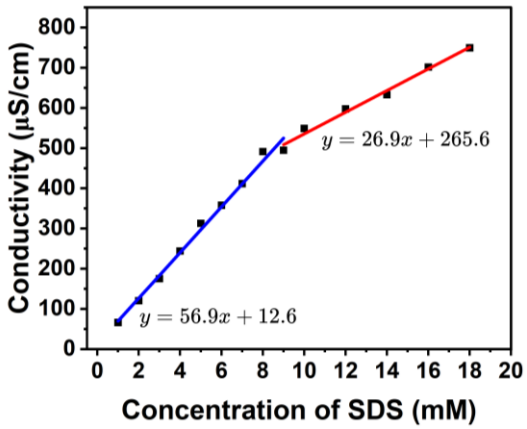

Figure 6-2. Conductivity of water as the SDS concentration increases. The concentration of SDS in the water medium was found to be 8.57 mM

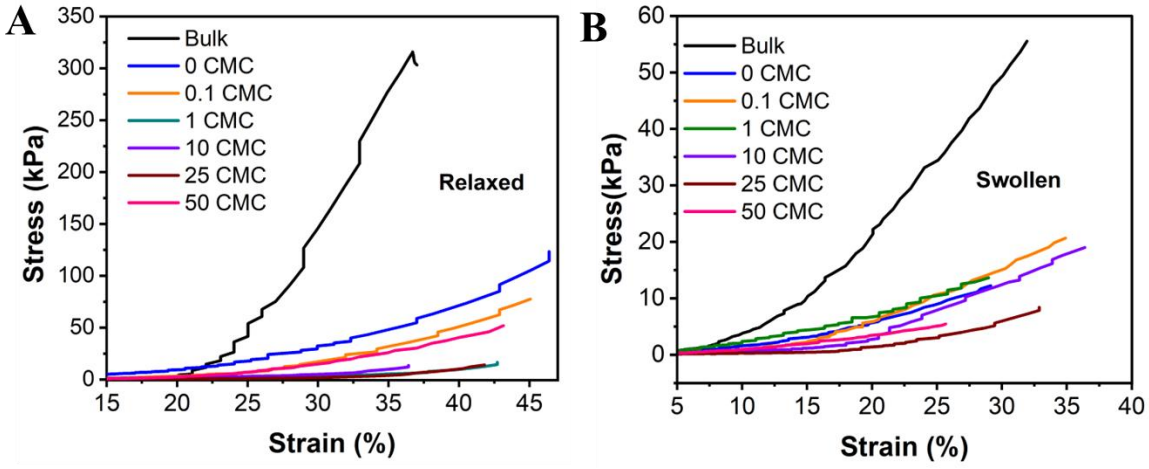

Figure 6-3. Stress vs Strain for the hydrogels at the relaxed state (A) and the swollen state (B)

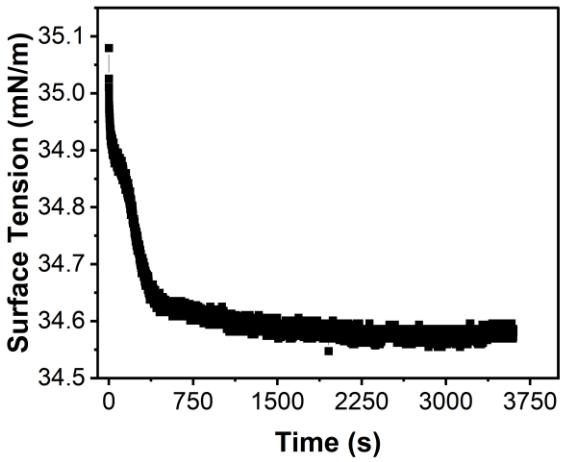

Figure 6-4. The surface tension was tested, and it was found to be 34.77 mN/m which is the same as the surface tension of SDS by itself at 25 CMC.

6.2 ^{1}H-NMR

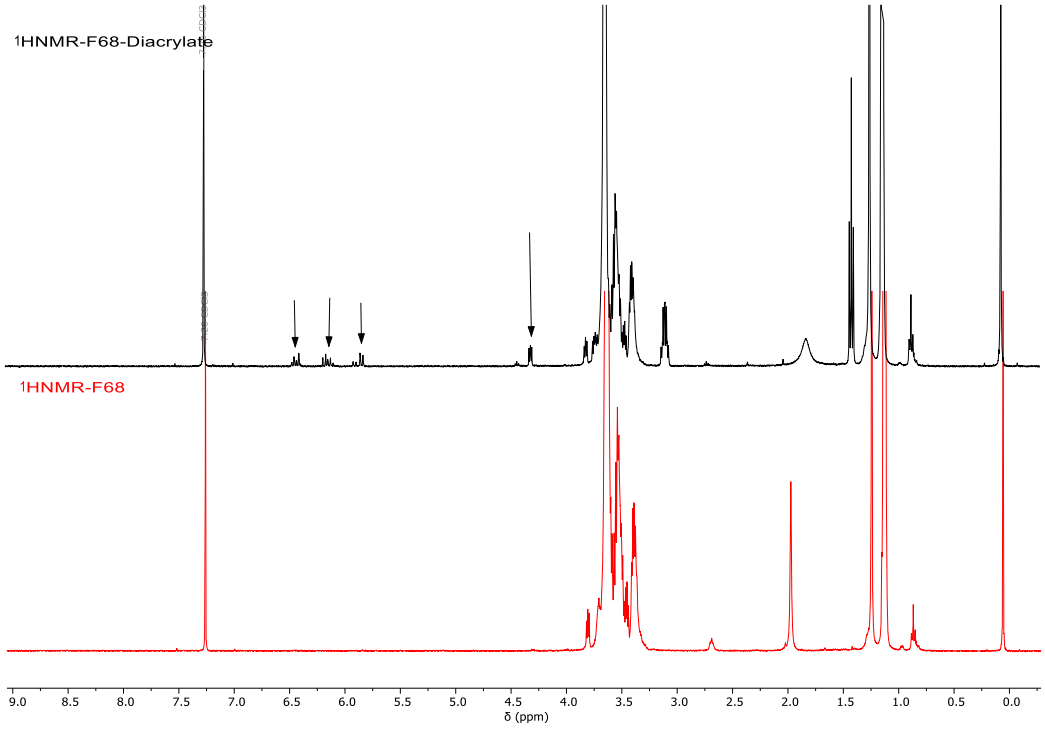

Figure 6-5. ^{1}H-NMR Results for PF68DA (Top) and PF68 (Bottom)

The results from ^{1}H-NMR in Figure 6-5 shows the presence of peaks around 5.5-6.5 ppm which is the signal for the acrylate peaks ($CH_2 = CH -$). The CH_2 usually appears around 5.8-6.1 ppm as a doublet because of the adjacent CH and around 6.1-6.5 ppm we have the CH which appears as a multiplet, which represent the vinyl protons of the acrylate groups with the double bond. The peaks found around 3.2-4.0 ppm is for the PEO ($-OCH_2CH_2O-$) chain and and the PPO protons ($-CH_2CH(CH_3)O-$). The signals around 1.0-1.5 ppm correspond to the methylene protons in the PPO block especially the ($-CH_2-$) that are next to the methyl gorups in the PPO structure. Between 0.8-1.2 ppm, the peaks correspond to the methyl groups in the PPO block (-CH_3-) The same peaks were reported in the literature. The integration was done for these peaks and the formula below was derived as a way to calculate the degree of acrylation inspired by this paper. The number of PO is 30 and of EO is 2 x 75 in PF68 at 8400 g/mol. After integration, the degree of acrylation was 75%.

6.3 Additional Calculations

PF68 Mole Calculation: $\text{n of F68} = \frac{50\text{g}}{8400\text{g/mol}} = 0.00595 \text{ mol}$

$$\text{n of OH} = 0.00595 \text{ mol} \times 2 = 0.0119 \text{ mol}$$

Triethylamine volume calculation : $2 \times \text{nOH} = 0.0238 \text{ mol}$

$$\text{mass} = 0.0238 \text{ mol} \times 101.191 \text{ g/mol} = 2.409\text{g}$$

$$\text{volume} = \frac{2.409 \text{ g}}{0.726\text{g/ml}} = 3.3 \text{ ml}$$

Acryloyl chloride Volume calculation

$$1.5 \times \mathrm{nOH} = 0.01785 \text{ mol}$$

$$\text{mass} = 0.01785 \text{ mol} \times 90.51 \frac{\text{g}}{\text{mol}} = 1.616\text{g}$$

$$\text{volume} = \frac{1.616 \text{ g}}{1.119\text{g/ml}} = 1.4 \text{ ml}$$